

# A Moving-Wave Implementation in WRF to Study the Impact of Surface Water Waves on the Atmospheric Boundary Layer

PEIYUN ZHU <sup>a</sup>, TIANYI LI<sup>a,b</sup>, JEFFREY D. MIROCHA<sup>c</sup>, ROBERT S. ARTHUR<sup>c</sup>, ZHAO WU<sup>c</sup>, AND OLIVER B. FRINGER<sup>a</sup>

<sup>a</sup> *Department of Civil and Environmental Engineering, Stanford University, Stanford, California*

<sup>b</sup> *Saint Anthony Falls Laboratory, University of Minnesota, Minneapolis, Minnesota*

<sup>c</sup> *Atmosphere, Earth and Energy Division, Lawrence Livermore National Laboratory, Livermore, California*

(Manuscript received 10 April 2023, in final form 12 August 2023, accepted 15 August 2023)

**ABSTRACT:** While numerous modeling studies have focused on the interaction of ocean surface waves with the atmospheric boundary layer, most employ idealized waves that are either monochromatic or synthetically generated from a theoretical wave spectrum, and the atmospheric solvers are typically incompressible. To study wind–wave coupling in real-world scenarios, a model that can simulate both realistic meteorological and wave conditions is necessary. In this paper we describe the implementation of a moving bottom boundary condition into the Weather Research and Forecasting Model for large-eddy simulation applications. We first describe the moving bottom boundary conditions within WRF’s pressure-based vertical coordinate system. We then validate our code with idealized test cases that have analytical solutions, including flow over a monochromatic wave with and without viscosity. Finally, we present results from turbulent flows over a moving monochromatic wave with different wave ages, and demonstrate satisfactory agreement of the wave growth rate with results from the literature. We also compare atmospheric stress and wind parameters from two physically equivalent cases. The first specifies a wind moving in the same direction as a propagating wave, while the second involves a stationary wave with the wind adjusted such that the wind relative to the wave is the same as in the first case. Results indicate that the velocity and Reynolds stress profiles for the two cases match, further validating the moving bottom implementation.

**KEYWORDS:** Boundary conditions; Model evaluation/performance; Air–sea interaction

## 1. Introduction

Ocean surface waves play a key role in the dynamics of the marine atmospheric boundary layer (ABL), impacting the winds and scalar concentrations within the ABL by modulating the momentum exchange and scalar fluxes at the air–sea interface (D’Asaro and McNeil 2007). Understanding the interaction between ocean surface waves and the ABL has important ramifications for both fundamental science and engineering, including parameterization of wave impacts in weather and climate modeling (Large et al. 1994), marine weather predictions and offshore wind energy assessment (Yang et al. 2014a,b; Xiao and Yang 2019).

The effect of waves on the wind field depends on various wave properties, including wave steepness (characterized by  $ka$ , where  $k$  is the wavenumber and  $a$  is the wave amplitude), wave age (defined as  $c/U_0$  or  $c/u_*$ , where  $c$  is the phase speed of the wave,  $U_0$  is a characteristic velocity of the wind, and  $u_*$  is the friction velocity of the wind) (Sullivan et al. 2000, 2014, 2018b,a), propagation direction (Patton et al. 2019; Husain et al. 2022a; Cao et al. 2020) and the angle of misalignment between the wave and the wind (Patton et al. 2019; Husain et al. 2022b; Deskos et al. 2022). Both observational and numerical studies have demonstrated the dependence of the mean wind profile, the drag coefficient, and wave growth rate

on waves with different properties (e.g., Plant 1982; Cheung and Street 1988; Reichl et al. 2014; Buckley and Veron 2016; Kumar et al. 2022), indicating the importance of wind–wave interaction on understanding the mechanisms of wave formation, air–sea exchange of momentum and energy, and parameterizing the effect of waves in large-scale models that cannot resolve the waves explicitly.

Wind–wave interaction has been studied with both one- and two-way coupled numerical models. In one-way coupling, the wave field is imposed as a bottom boundary condition affecting the airflow, yet the waves are not influenced by the wind. Different types of waves have been employed in one-way coupling studies, including a monochromatic linear sinusoidal wave (e.g., Sullivan et al. 2000; Zhang et al. 2019; Cao and Shen 2021), Stokes waves (e.g., Yang and Shen 2011a; Druzhinin et al. 2019; Cao et al. 2023), and broadband waves (e.g., Sullivan et al. 2014, 2018a). In one-way coupling between broadband waves and airflow, researchers further neglect nonlinear wave–wave interactions and superimpose broadband linear wave components to accelerate computational speed (Sullivan et al. 2014, 2018b). Both direct numerical simulation (DNS) and large-eddy simulation (LES) have been employed in one-way coupled models, using a curvilinear coordinate that maps the grid to the shape of the moving waves (e.g., Sullivan et al. 2000, 2014; Zhang et al. 2019). These studies focus on the wave-induced effects on the mean wind profile, shear stress, and turbulence characteristics. In two-way coupled models, the wind and the wave are coupled dynamically and evolve together. Existing two-way coupled models use either a curvilinear coordinate (e.g., Yang and Shen 2011a,b; Li and Shen 2022b) or the volume-of-fluid method (e.g., Campbell et al. 2016;

 Denotes content that is immediately available upon publication as open access.

Corresponding author: Peiyun Zhu, zhpyun@stanford.edu

DOI: 10.1175/MWR-D-23-0077.1

© 2023 American Meteorological Society. This published article is licensed under the terms of the default AMS reuse license. For information regarding reuse of this content and general copyright information, consult the AMS Copyright Policy ([www.ametsoc.org/PUBSReuseLicenses](http://www.ametsoc.org/PUBSReuseLicenses)).

Cimarelli et al. 2023; Wu and Deike 2021) to resolve the two-phase flow. The majority of the two-way coupling studies employ DNS and focus on the small-scale dynamics of nonlinear wave–wave interaction, turbulence on the waterside, scalar transfer across the interface or wind–wave generation (Lin et al. 2008; Liu et al. 2009; Komori et al. 2010; Campbell et al. 2016; Wu and Deike 2021; Li and Shen 2022a,b). Although two-way coupled models resolve the influence of the wind on waves, they are computationally expensive and limited to small-scale dynamics at relatively low Reynolds numbers. They require complicated boundary conditions on the deformable water surface to enforce continuous velocity and stress profiles, and result in high computational costs (Yang and Shen 2011b; Campbell et al. 2016). Hao and Shen (2019) built an LES tool to simulate two-way coupled wind and wave fields. In their model, waves are simulated with a high-order spectral (HOS) method developed by Dommermuth and Yue (1987). This method captures both the evolution of phase-resolved waves under the influence of the wind and the nonlinear interaction between waves. Hao and Shen (2019) showed that the nonlinear interactions, rather than the influence of the wind, play the dominant role in the long-term wave evolution. The HOS wave solver needs to have a finer grid and smaller time step than the LES model because nonlinear wave–wave interaction transfers energy to higher frequencies. This increases the computational cost of the two-way coupled LES–HOS model, and the grid size mismatch between the LES and HOS models further complicates the implementation of the coupling. Moreover, Yang and Shen (2009) compared one- and two-way coupled DNS simulation results and found negligible differences in airflow vortical structures between the two. These results suggest that the one-way coupled model can provide satisfactory fidelity much more efficiently than a two-way coupled model for the study of wave effects on airflow and turbulence.

Studies using either one- or two-way coupled models have revealed important wave-induced effects on the ABL. Sullivan et al. (2000) showed that monochromatic waves can increase the turbulent momentum flux near the wave surface by as much as 40% compared to a flat surface. Using the LES–HOS model initialized with a wave field generated by an empirical ocean spectrum, Hao and Shen (2019) found that the streamwise velocity spectrum of the wind displays a clear wave signature that follows the dispersion relation for deep water waves, but this signature is restricted to a height dictated by the peak wavelength. The one-way coupled model has been used to show that ocean swells can increase the overall wind power extraction in offshore wind farms by as much as 18% in low wind speed conditions when the waves act to increase the wind speed (Yang et al. 2014a,b). Hao et al. (2018) utilized the same coupled model to explore the interactions between airflow and wave groups and found that the presence of long waves can reduce the form drag of short waves. This model has also been applied for simulating wind over fast-propagating monochromatic waves, revealing that the vertical component of the wave orbital velocity dominates the wave-induced airflow perturbation (Cao and Shen 2021). More recently, several one-way coupled numerical studies have focused on wind-opposing

wave or misaligned wind and waves. Cao et al. (2023) used LES with prescribed Stokes waves and theoretical analysis to show that for fast opposing waves, wave-induced airflow perturbation is dominated by the linear response of the wind to the wave. Deskos et al. (2022) used DNS with linear, monochromatic sine waves of different phase speeds and directions relative to the wind. They reported a large deviation in the mean velocity vector relative to the applied pressure gradient when fast-moving waves were aligned at an angle of 135° relative to the applied pressure gradient vector. However, this DNS study is limited to a very low Reynolds number, similar to other two-way coupled DNS studies focusing on small-scale features such as the wave-induced Stokes sublayer (Cimarelli et al. 2023) and wind–wave growth mechanisms (Li and Shen 2022a,b; Wu et al. 2022).

The studies mentioned above have explored many aspects of wind–wave interaction. However, the simulations are limited to idealized or synthetic atmospheric conditions lacking important meteorological factors such as temperature stratification, humidity, and radiation. To develop a comprehensive understanding of the interaction between ocean surface waves and the ABL, a coupled wind–wave model that can simulate realistic meteorological and wave conditions is needed. A good candidate for realistic wind simulations is the Weather Research and Forecasting (WRF) Model. WRF is a widely used mesoscale numerical weather prediction model for both atmospheric research and operational applications (Skamarock et al. 2008). WRF solves the compressible Navier–Stokes equations with Coriolis terms and includes transport equations for temperature, moisture, and tracers. Using a pressure-based curvilinear coordinate, WRF can simulate flow over complex terrain with moderate slopes and over multiple scales from turbulence-resolving to synoptic. At large scales, WRF can be forced by numerous meteorological datasets and provides multiple numerical solution options as well as physics parameterizations for land surface, planetary boundary layer, atmospheric and surface radiation, microphysics, and cumulus convection. At small scales, an LES capability is also available with different subgrid-scale turbulence options. WRF also provides a grid-nesting mesh refinement option that enables LES domains to be placed within mesoscale bounding-domain simulations, permitting small-scale process studies to be conducted within realistic mesoscale flows forced by real data. Moreover, WRF's two-way nesting capability provides a tool to fully couple different scales with both up-sale and down-scale information exchange at nested domain boundaries.

Given these capabilities, coupling WRF–LES with phase-resolved moving surface waves can enable comprehensive numerical studies of the influence of surface waves on the ABL in both idealized and realistic meteorological and oceanographic settings. These studies will benefit larger-scale atmosphere–wave modeling by aiding the improvement of drag parameterization for wind over surface water waves. In fact, Yang et al. (2013) developed a dynamic model of sea surface roughness using a two-way coupled LES–HOS model. A recent study proposed a less computationally expensive sea surface based drag model for LES of wind over waves, which is only applicable to monochromatic sinusoidal waves with a

known phase speed and wave steepness (Aiyer et al. 2023). The coupled wave and WRF-LES model can be used to study drag parameterization under more realistic scenarios and extend the functionality of existing drag parameterization. Another potential application of the coupled wave and WRF-LES model is to improve offshore wind energy prediction. Castorrini et al. (2023) recently coupled a mesoscale numerical weather prediction model with a local-scale Reynolds-averaged Navier-Stokes (RANS) model to investigate offshore wind turbine inflow. Since wave effects are parameterized in their model, a coupled wave and WRF-LES model could improve the effect of the waves on the wind. In this manner, a coupled wave and WRF-LES model will be able to provide more accurate multi-fidelity simulation results for offshore wind energy applications.

As the current WRF model’s surface elevation boundary condition does not permit time-variability, this paper presents an implementation of a moving bottom to represent propagating water waves. The method is validated with test cases including laminar and turbulent flow over both stationary and moving sine waves. The paper is organized as follows: section 2 describes in detail the vertical coordinate and governing equations in WRF, followed by the moving bottom implementation; section 3 presents results of two laminar flow test cases and turbulent flow test cases with three different wave ages; and finally, section 4 summarizes the results and discusses future work.

## 2. Methods

### a. Governing equations in WRF

Although details of the WRF equations can be found in Skamarock et al. (2008), we repeat many of the equations here in order to clearly demonstrate the implementation of the moving bottom. WRF solves the compressible Navier-Stokes equations in a pressure-based curvilinear coordinate system defined by

$$\tau = t, \quad \xi = x, \quad \eta = y, \quad \zeta = \frac{p_h - p_{h,top}}{\mu}, \quad (1)$$

where  $\tau$  is the time coordinate of the curvilinear system,  $\xi$  and  $\eta$  are the horizontal curvilinear coordinates, and  $\zeta$  is the pressure-based vertical coordinate. The subscript  $h$  denotes hydrostatic variables,  $\mu = p_{h,s} - p_{h,top}$  is the difference between the hydrostatic pressure at the surface,  $p_{h,s}$ , and the hydrostatic pressure at the top of the domain,  $p_{h,top}$ , hence, represents the dry air mass per unit area. A schematic of the coordinate system is given in Fig. 1. The spatial discretization in WRF adopts C grid staggering, with velocities staggered one-half grid length from the thermodynamic variables located in the cell centers, as shown in Fig. 2. We note that starting from version 4, WRF uses a hybrid sigma-pressure vertical coordinate that generalizes the pressure-based vertical coordinate to reduce the influence of the terrain more rapidly with increasing height (Skamarock et al. 2019). When this hybrid coordinate is employed, the definition of  $\zeta$  is modified based on Eq. (1). Nevertheless, the moving bottom implementation

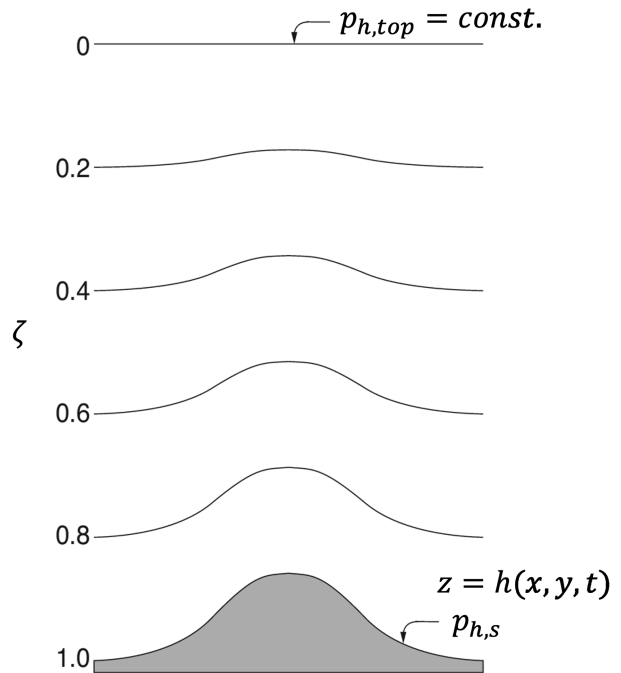


FIG. 1. The pressure-based curvilinear coordinate in WRF, adapted from Skamarock et al. (2008), with the bottom represented by a moving surface at  $z = h(x, y, t)$ .

discussed in this section can be easily adapted to the hybrid coordinate, and hence we restrict our discussion to the original pressure-based coordinate in the present study.

To write the governing equations in conservative flux form, conservative fluxes are defined as

$$\mathbf{U} = \mu \mathbf{u} = (U, V, W), \quad (2)$$

where  $\mathbf{u}$  is the Cartesian velocity vector. The cross-coordinate flux is defined as

$$\Omega = \mu \frac{d\zeta}{dt}. \quad (3)$$

Noting the metrics of coordinate transformation

$$\frac{\partial \zeta}{\partial t} = -J \frac{\partial z}{\partial \tau}, \quad (4a)$$

$$\frac{\partial \zeta}{\partial x} = -J \frac{\partial z}{\partial \xi}, \quad (4b)$$

$$\frac{\partial \zeta}{\partial y} = -J \frac{\partial z}{\partial \eta}, \quad (4c)$$

where the determinant of the matrix of transformation, or the Jacobian, is given by

$$\frac{\partial \zeta}{\partial z} = J, \quad (5)$$

the cross-coordinate flux can be written as

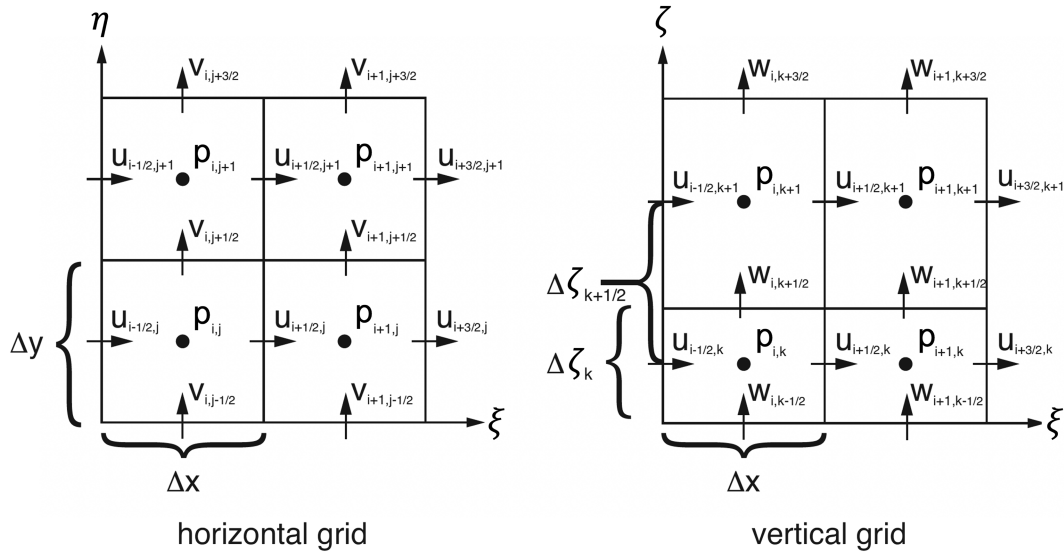


FIG. 2. The grid in WRF, adapted from Skamarock et al. (2008), where  $(i, j, k)$  are the indices of grid points in the  $(\xi, \eta, \zeta)$  directions.

$$\Omega = \mu \left( \frac{\partial \zeta}{\partial t} + u \frac{\partial \zeta}{\partial x} + v \frac{\partial \zeta}{\partial y} + w \frac{\partial \zeta}{\partial z} \right) = J \left( W_n - \mu \frac{\partial z}{\partial \tau} \right), \tag{6}$$

where the conservative flux normal to  $\zeta$  surfaces is given by

$$W_n = W - U \frac{\partial z}{\partial \xi} - V \frac{\partial z}{\partial \eta}. \tag{7}$$

Defining the nonconservative geopotential  $\phi = gz$ , the pressure  $p$ , and inverse density  $\alpha = 1/\rho$ , the momentum equations in the pressure-based curvilinear coordinate system are given by

$$\frac{\partial U}{\partial \tau} + \frac{\partial}{\partial \xi} (Uu) + \frac{\partial}{\partial \eta} (Vu) + \frac{\partial}{\partial \zeta} (\Omega u) + \mu \alpha \frac{\partial p}{\partial \xi} + \frac{\partial p}{\partial \zeta} \frac{\partial \phi}{\partial \xi} = F_U, \tag{8a}$$

$$\frac{\partial V}{\partial \tau} + \frac{\partial}{\partial \xi} (Uv) + \frac{\partial}{\partial \eta} (Vv) + \frac{\partial}{\partial \zeta} (\Omega v) + \mu \alpha \frac{\partial p}{\partial \eta} + \frac{\partial p}{\partial \zeta} \frac{\partial \phi}{\partial \eta} = F_V, \tag{8b}$$

$$\frac{\partial W}{\partial \tau} + \frac{\partial}{\partial \xi} (Uw) + \frac{\partial}{\partial \eta} (Vw) + \frac{\partial}{\partial \zeta} (\Omega w) - g \left( \frac{\partial p}{\partial \zeta} - \mu \right) = F_W, \tag{8c}$$

where  $F_U, F_V$ , and  $F_W$  are the forcing terms that include turbulent mixing, Coriolis force, buoyancy, and model physics, respectively (e.g., microphysics of clouds, radiation, and planetary boundary layer models). The transformed equation governing conservation of mass is given by

$$\frac{\partial \mu}{\partial \tau} + \frac{\partial U}{\partial \xi} + \frac{\partial V}{\partial \eta} + \frac{\partial \Omega}{\partial \zeta} = 0, \tag{9}$$

and the kinematic condition or the geometric conservation law (GCL) is given by

$$\frac{\partial \phi}{\partial \tau} + \frac{1}{\mu} \left( U \frac{\partial \phi}{\partial \xi} + V \frac{\partial \phi}{\partial \eta} + \Omega \frac{\partial \phi}{\partial \zeta} - gW \right) = 0. \tag{10}$$

The equation of state is given by

$$p = p_0 (R\theta/p_0\alpha)^\gamma, \tag{11}$$

where  $p_0 = 10^5$  Pa is a reference atmospheric pressure,  $R$  is the ideal gas constant for dry air,  $\gamma = c_p/c_v = 1.4$  is the ratio of heat capacities for dry air, and because we restrict our study to a neutral ABL, the potential temperature is assumed to be constant and given by  $\theta = 300$  K.

Finally, the hydrostatic balance is derived as

$$\frac{\partial \phi}{\partial \zeta} = \frac{\partial \phi}{\partial z} \frac{\partial z}{\partial p_h} \frac{\partial p_h}{\partial \zeta} = g \left( -\frac{1}{\rho g} \right) \mu = -\mu \alpha. \tag{12}$$

In Eqs. (8)–(12), we omitted the map factors used to project the computational domain onto the curved surface of Earth as we aim to study small-scale flows with LES in which the curvature of Earth does not play a role. We also do not consider moisture in this study, and thus do not distinguish between the density of moist and dry air.

To reduce errors associated with numerical truncation and finite-precision arithmetic in the pressure gradient and buoyancy terms, WRF solves the perturbation form of Eqs. (8)–(12), whereby the perturbation variables are given by their departures from a hydrostatic background state (denoted by the overbar), such that

$$p' = p - \bar{p}(x, y, \bar{z}, t), \tag{13a}$$

$$\phi' = \phi - \bar{\phi}(x, y, \bar{z}, t), \tag{13b}$$

$$\alpha' = \alpha - \bar{\alpha}(x, y, \bar{z}, t), \tag{13c}$$

$$\mu' = \mu - \bar{\mu}(x, y, \bar{z}, t). \tag{13d}$$

Substitution into the governing equations gives

$$\begin{aligned} \frac{\partial U}{\partial \tau} + \frac{\partial}{\partial \xi}(Uu) + \frac{\partial}{\partial \eta}(Vu) + \frac{\partial}{\partial \zeta}(\Omega u) + \mu \left( \frac{\partial \phi'}{\partial \xi} + \alpha \frac{\partial p'}{\partial \xi} + \alpha' \frac{\partial \bar{p}}{\partial \xi} \right) \\ + \frac{\partial \phi}{\partial \xi} \left( \frac{\partial p'}{\partial \zeta} - \mu' \right) = F_U, \end{aligned} \tag{14a}$$

$$\begin{aligned} \frac{\partial V}{\partial \tau} + \frac{\partial}{\partial \xi}(Uv) + \frac{\partial}{\partial \eta}(Vv) + \frac{\partial}{\partial \zeta}(\Omega v) + \mu \left( \frac{\partial \phi'}{\partial \eta} + \alpha \frac{\partial p'}{\partial \eta} + \alpha' \frac{\partial \bar{p}}{\partial \eta} \right) \\ + \frac{\partial \phi}{\partial \eta} \left( \frac{\partial p'}{\partial \zeta} - \mu' \right) = F_V, \end{aligned} \tag{14b}$$

$$\frac{\partial W}{\partial \tau} + \frac{\partial}{\partial \xi}(Uw) + \frac{\partial}{\partial \eta}(Vw) + \frac{\partial}{\partial \zeta}(\Omega w) - g \frac{\partial p'}{\partial \zeta} + \mu' g = F_W, \tag{14c}$$

$$\frac{\partial \mu'}{\partial \tau} + \frac{\partial U}{\partial \xi} + \frac{\partial V}{\partial \eta} + \frac{\partial \Omega}{\partial \zeta} = 0, \tag{14d}$$

$$\frac{\partial \phi'}{\partial \tau} + \frac{1}{\mu} \left( U \frac{\partial \phi}{\partial \xi} + V \frac{\partial \phi}{\partial \eta} + \Omega \frac{\partial \phi}{\partial \zeta} - gW \right) = 0, \tag{14e}$$

$$\frac{\partial \phi'}{\partial \zeta} = -\bar{\mu} \alpha' - \mu' \bar{\alpha}. \tag{14f}$$

We note that Eqs. (14a)–(14f) are exact. They are derived without approximation or dropping high-order terms.

For time advancement, WRF uses the Runge–Kutta (RK) method. Each RK step is divided into a number of acoustic steps that update the acoustic equations. The number of acoustic steps can be defined by the user based on the CFL condition related to advection and propagation of sound waves, as discussed in section 2d.

The acoustic step equations solve for the evolution of the deviations of the variables from their most recent RK predictor step, denoted by the superscript  $i^*$ , such that

$$\mathbf{U}'' = \mathbf{U} - \mathbf{U}^{i^*}, \tag{15a}$$

$$\Omega'' = \Omega - \Omega^{i^*}, \tag{15b}$$

$$\phi'' = \phi - \phi^{i^*}, \tag{15c}$$

$$\alpha'' = \alpha - \alpha^{i^*}, \tag{15d}$$

$$\mu'' = \mu - \mu^{i^*}. \tag{15e}$$

The governing equations for the acoustic time-substepping are given by

$$\begin{aligned} \frac{\partial \mathbf{U}''}{\partial \tau_a} + \mu^{i^*} \left( \frac{\partial \phi''^{\tau_a}}{\partial \xi} + \alpha^{i^*} \frac{\partial p''^{\tau_a}}{\partial \xi} + \alpha''^{\tau_a} \frac{\partial \bar{p}}{\partial \xi} \right) + \frac{\partial \phi^{i^*}}{\partial \xi} \left( \frac{\partial p''}{\partial \zeta} - \mu' \right)^{\tau_a} \\ = R_U^{i^*} + F_U^{i^*}, \end{aligned} \tag{16a}$$

$$\begin{aligned} \frac{\partial V''}{\partial \tau_a} + \mu^{i^*} \left( \frac{\partial \phi''^{\tau_a}}{\partial \eta} + \alpha^{i^*} \frac{\partial p''^{\tau_a}}{\partial \eta} + \alpha''^{\tau_a} \frac{\partial \bar{p}}{\partial \eta} \right) + \frac{\partial \phi^{i^*}}{\partial \eta} \left( \frac{\partial p''}{\partial \zeta} - \mu' \right)^{\tau_a} \\ = R_V^{i^*} + F_V^{i^*}, \end{aligned} \tag{16b}$$

$$\frac{\partial W''}{\partial \tau_a} - g \left[ \frac{\partial}{\partial \zeta} \left( C \frac{\partial \phi''}{\partial \zeta} \right) - \mu'' \right]^{\tau_a} = R_W^{i^*}, \tag{16c}$$

$$\frac{\partial \mu''}{\partial \tau_a} + \left( \frac{\partial U''}{\partial \xi} + \frac{\partial V''}{\partial \eta} + \frac{\partial \Omega''}{\partial \zeta} \right)^{\tau_a + \Delta \tau_a} = R_\mu^{i^*}, \tag{16d}$$

$$\frac{\partial \phi''}{\partial \tau_a} + \frac{1}{\mu^{i^*}} \left( \Omega''^{\tau_a + \Delta \tau_a} \frac{\partial \phi^{i^*}}{\partial \zeta} - g \overline{W''}^{\tau_a} \right) = R_\phi^{i^*}, \tag{16e}$$

where  $\tau_a$  denotes discrete time levels in the acoustic steps,  $\Delta \tau_a$  is the acoustic time step,  $C = \alpha'^2 c_s^2 / u^{i^*}$  and  $c_s = \gamma p^{i^*} \alpha^{i^*}$  is the sound speed at step  $i^*$ . The discrete acoustic time-step operator for some quantity  $f$  is given by

$$\bar{f}^{\tau_a} = \frac{1 + \beta}{2} f^{\tau_a + \Delta \tau_a} + \frac{1 - \beta}{2} f^{\tau_a}, \tag{17}$$

where the implicitness parameter satisfies  $0 \leq \beta \leq 1$  and determines the degree of implicitness of the discrete time integration of Eqs. (16c) and (16e). If  $\beta = 0$ , the time marching scheme is Crank–Nicolson, while if  $\beta = 1$ , the scheme is the fully implicit backward Euler. A nonzero  $\beta$  damps instabilities associated with vertically propagating sound waves (Skamarock et al. 2008). The acoustic pressure  $p''$  is diagnosed with the linearized equation of state:

$$p'' = -\frac{c_s^2}{\alpha^{i^*}} \left( \frac{\alpha''}{\alpha^{i^*}} + \frac{\mu''}{\mu^{i^*}} \right). \tag{18}$$

The terms on the right-hand side of Eqs. (16a)–(16e) are given by

$$\begin{aligned} R_U^{i^*} = - \left[ \frac{\partial}{\partial \xi}(Uu) + \frac{\partial}{\partial \eta}(Vu) + \frac{\partial}{\partial \zeta}(\Omega u) \right] \\ - \left[ \mu \left( \frac{\partial \phi'}{\partial \xi} + \alpha \frac{\partial p'}{\partial \xi} + \alpha' \frac{\partial \bar{p}}{\partial \xi} \right) + \frac{\partial \phi}{\partial \xi} \left( \frac{\partial p'}{\partial \zeta} - \mu' \right) \right] + F_U, \end{aligned} \tag{19a}$$

$$\begin{aligned} R_V^{i^*} = - \left[ \frac{\partial}{\partial \xi}(Uv) + \frac{\partial}{\partial \eta}(Vv) + \frac{\partial}{\partial \zeta}(\Omega v) \right] \\ - \left[ \mu \left( \frac{\partial \phi'}{\partial \eta} + \alpha \frac{\partial p'}{\partial \eta} + \alpha' \frac{\partial \bar{p}}{\partial \eta} \right) + \frac{\partial \phi}{\partial \eta} \left( \frac{\partial p'}{\partial \zeta} - \mu' \right) \right] + F_V, \end{aligned} \tag{19b}$$

$$R_W^{i^*} = - \left[ \frac{\partial}{\partial \xi}(Uw) + \frac{\partial}{\partial \eta}(Vw) + \frac{\partial}{\partial \zeta}(\Omega w) \right] + g \frac{\partial p'}{\partial \zeta} - \mu' g + F_W, \tag{19c}$$

$$R_\mu^{i^*} = - \left( \frac{\partial U}{\partial \xi} + \frac{\partial V}{\partial \eta} + \frac{\partial \Omega}{\partial \zeta} \right), \tag{19d}$$

$$R_\phi^{t^*} = -\frac{1}{\mu} \left( U \frac{\partial \phi}{\partial \xi} + V \frac{\partial \phi}{\partial \eta} + \Omega \frac{\partial \phi}{\partial \zeta} - gW \right), \quad (19e)$$

where all values are evaluated at time step  $t^*$ . The acoustic form of the hydrostatic relation is given by

$$\frac{\partial \phi''}{\partial \zeta} = -\alpha'' \mu^{t^*} - \alpha^* \mu''. \quad (20)$$

In summary, the acoustic step equations are advanced explicitly by the RK method, except that Eqs. (16c) and (16e) are solved semi-implicitly. Also,  $\mu''$  is advanced after  $U$ ,  $V$ , and  $\Omega$  are updated for step  $\tau_a + \Delta\tau_a$ , and thus Eq. (16d) is explicitly solved. Boundary conditions at the sea surface ( $\zeta = 1$ ) are needed for Eqs. (16a)–(16e) as discussed in what follows.

### b. Moving bottom implementation

The implementation of a moving bottom in WRF is divided into two parts. The first is to specify boundary conditions, and the second is to update the hydrostatic balance at each time step as the bottom moves.

#### 1) BOTTOM BOUNDARY CONDITIONS

We define the location of the water surface as  $z = h$ , which is also the surface defined by  $\zeta = 1$ . Since the vertical velocity across the air–sea interface should be continuous, we require

the vertical velocity of the water surface to match the air velocity at the surface, such that

$$w|_{z=h} = \frac{dh}{dt} = \frac{\partial h}{\partial \tau} + u|_{\zeta=1} \frac{\partial h}{\partial \xi} + v|_{\zeta=1} \frac{\partial h}{\partial \eta}. \quad (21)$$

Since  $\phi = gz$ , the kinematic boundary condition [Eq. (21)] at the water surface in terms of the geopotential is

$$gw|_{z=h} = \left( \frac{\partial \phi}{\partial \tau} + u \frac{\partial \phi}{\partial \xi} + v \frac{\partial \phi}{\partial \eta} \right) \Big|_{\zeta=1}. \quad (22)$$

From Eq. (6), the cross-coordinate flux at the water surface is then given by

$$\begin{aligned} \Omega|_{\zeta=1} &= J \left( W_n - \mu \frac{\partial \xi}{\partial \tau} \right) \\ &= \mu J \left( w|_{\zeta=1} - u|_{\zeta=1} \frac{\partial h}{\partial \xi} - v|_{\zeta=1} \frac{\partial h}{\partial \eta} - \frac{\partial h}{\partial \tau} \right) \end{aligned} \quad (23a)$$

$$= 0. \quad (23b)$$

Equations (22) and (23b) are the general boundary conditions for a moving bottom in a curvilinear coordinate system. The specific implementation in WRF, however, requires that the boundary conditions for  $\phi$  and  $w$  are consistent with Eqs. (16e) and (16c). To this end, Eq. (16e) is discretized semi-implicitly in time with

$$\frac{\phi''^{\tau_a + \Delta\tau_a} - \phi''^{\tau_a}}{\Delta\tau_a} + \frac{1}{\mu^{t^*}} \left[ \Omega''^{\tau_a + \Delta\tau_a} \frac{\partial \phi^*}{\partial \zeta} - g \left( \frac{1 + \beta}{2} W''^{\tau_a + \Delta\tau_a} + \frac{1 - \beta}{2} W''^{\tau_a} \right) \right] = -\frac{1}{\mu^{t^*}} \left( U^{t^*} \frac{\partial \phi^*}{\partial \xi} + V^{t^*} \frac{\partial \phi^*}{\partial \eta} + \Omega^* \frac{\partial \phi^*}{\partial \zeta} - gW^{t^*} \right). \quad (24)$$

In practice,  $\beta = 1$  gives a good balance between stability and accuracy for moving bottom applications.

Since  $\Omega = \Omega'' = 0$  at  $z = h(x, y, t)$ , Eq. (24) can be used to solve for  $W''^{\tau_a + \Delta\tau_a}$  at  $z = h(x, y, t)$ , such that

$$\begin{aligned} W''^{\tau_a + \Delta\tau_a} &= \frac{2}{1 + \beta} \left( \mu^{t^*} \frac{h^{\tau_a + \Delta\tau_a} - h^{\tau_a}}{\Delta\tau_a} + U^{t^*} \frac{\partial h^*}{\partial \xi} + V^{t^*} \frac{\partial h^*}{\partial \eta} - W^{t^*} \right. \\ &\quad \left. - \frac{1 - \beta}{2} W''^{\tau_a} \right). \end{aligned} \quad (25)$$

Because  $h$  is prescribed,  $h^{\tau_a + \Delta\tau_a}$  and  $h^{\tau_a}$  are known. Therefore, Eq. (25) can be used to compute  $W''^{\tau_a + \Delta\tau_a}$  at  $z = h(\tau_a + \Delta\tau_a, x, y)$ , and then  $\phi''^{\tau_a + \Delta\tau_a}$  at  $z = h(\tau_a + \Delta\tau_a, x, y)$  can be computed by using the value of  $W''^{\tau_a + \Delta\tau_a}$  in Eq. (24).

Boundary conditions for the horizontal velocities depend on the flow condition. For inviscid flow, the horizontal velocity of the air is free-slip at the bottom, and hence horizontal velocity information from the wave is not needed. For viscous flow, the horizontal velocities are continuous across the interface, i.e., Dirichlet boundary conditions should be applied. For a rough wall, the original WRF–LES code has a quadratic drag law at the bottom, which is modified to account for a moving bottom by computing the stress based on the velocity

of the air relative to the velocity of the water, such that the relative velocity at  $z = h$  is given by

$$\mathbf{u}_r = \mathbf{u} - \mathbf{u}_w, \quad (26)$$

where  $\mathbf{u}_w$  is the velocity of the water at  $z = h$ . Defining the components of velocity parallel to the water surface as

$$u_{\parallel} = \frac{u_r + w_r (\partial h / \partial \xi)}{\sqrt{(\partial h / \partial \xi)^2 + 1}}, \quad (27a)$$

$$v_{\parallel} = \frac{v_r + w_r (\partial h / \partial \eta)}{\sqrt{(\partial h / \partial \eta)^2 + 1}}, \quad (27b)$$

the horizontal components of the stress by the water on the flow are given by

$$\tau_{13} = C_d |\mathbf{u}_r| u_{\parallel}, \quad (28a)$$

$$\tau_{23} = C_d |\mathbf{u}_r| v_{\parallel}, \quad (28b)$$

where the drag coefficient  $C_d$  ensures that the horizontal velocity in the bottom-most WRF grid cell (at  $z = h + \Delta z/2$ ) satisfies the log law, such that

$$C_d = \left[ \frac{\kappa}{\ln \Delta z / (2z_0)} \right]^2, \tag{29}$$

where  $\kappa = 0.4$  is the von Kármán constant and  $z_0$  is the roughness height. We use  $z_0 = 0.0002$  m, which is a typical roughness height value for the low wind marine boundary layer (Sullivan et al. 2008). This implementation of the quadratic drag law for a moving wavy bottom is consistent with previous numerical studies (e.g., Yang et al. 2013; Sullivan et al. 2014; Hao and Shen 2019).

## 2) HYDROSTATIC REBALANCING

In the original WRF code, the hydrostatic variables  $\bar{p}$ ,  $\bar{\phi}$ ,  $\bar{\alpha}$ , and  $\bar{\mu}$  are fixed in time since they are based on the height of a stationary bottom, except for moving nested domains that typically evolve over synoptic time scales. With surface water waves, however, the height of each grid point changes as the wave height changes, and therefore the hydrostatic variables at each grid point also change. With waves with small steepness, although the change is small, recomputing the hydrostatic variables gives a more accurate representation of the hydrostatic pressure gradient terms in Eqs. (16a), (16b), (19a), and (19b), which improves the accuracy of the simulation results. In the moving bottom implementation, this change in hydrostatic variables is addressed through the hydrostatic rebalancing procedure illustrated as follows.

At the end of each time step, we first update the hydrostatic variables at the bottom ( $z = h$  or  $\zeta = 1$ ). The geopotential height at the water surface is first updated based on the wave height at the next time step, such that

$$\phi_h^{t+\Delta t} \Big|_{\zeta=1} = gh^{t+\Delta t}, \tag{30}$$

after which  $\bar{p}|_{\zeta=1}$  and  $\bar{\mu}$  are linearly interpolated from a profile of hydrostatic pressure at different heights. Next, the hydrostatic pressure above the water surface is updated with Eq. (1), such that

$$\bar{p}_k^{t+\Delta t} = \zeta_k \bar{\mu}^{t+\Delta t} + p_{h,\text{top}}, \quad k \geq 2, \tag{31}$$

where  $k$  is the index of the vertical grid. Next, the inverse density is updated with the equation of state, Eq. (11), such that

$$\bar{\alpha}^{t+\Delta t} = \left( \frac{\bar{p}^{t+\Delta t}}{p_0} \right)^{-1/\gamma} \frac{R_d \theta}{p_0}, \tag{32}$$

and then  $\bar{\phi}$  is updated by integrating the hydrostatic Eq. (12) upward with

$$\bar{\phi}_k^{t+\Delta t} = \bar{\phi}_{k-1}^{t+\Delta t} - \Delta \zeta_{k-1} \bar{\mu} \bar{\alpha}_{k-1}, \quad k \geq 2. \tag{33}$$

Finally, the perturbation variables are updated with Eqs. (13a)–(13d), such that

$$\phi^{t+\Delta t} = \phi^t - \bar{\phi}^{t+\Delta t}, \tag{34a}$$

$$p^{t+\Delta t} = p^t - \bar{p}^{t+\Delta t}, \tag{34b}$$

$$\mu^{t+\Delta t} = \mu^t - \bar{\mu}^{t+\Delta t}, \tag{34c}$$

$$\alpha^{t+\Delta t} = \alpha^t - \bar{\alpha}^{t+\Delta t}. \tag{34d}$$

The resulting rebalanced hydrostatic and perturbation variables are then used to compute the terms in the governing equations at the next time step. If a hybrid sigma–pressure vertical coordinate is used instead of the pressure-based vertical coordinate, such as in WRF version 4 and onward, only Eq. (31) needs to be modified based on the definition of  $\zeta$  in the hybrid sigma–pressure vertical coordinate. The other numerical schemes in hydrostatic rebalancing and boundary conditions in the moving bottom implementation remain the same.

## c. Numerical procedure

The numerical procedure for the moving bottom implementation in WRF is summarized here, and is slightly modified from Skamarock et al. (2008). In each RK step, the forcing terms  $F_U$ ,  $F_V$ , and  $F_W$  and the  $R^r$  terms in Eqs. (16a)–(16e) are computed. Then we compute each acoustic step as follows:

- 1) Advance horizontal momentum with Eqs. (16a) and (16b), with boundary conditions (28a) and (28b) for a rough surface and free- or no-slip, otherwise.
- 2) Advance  $\mu''$  with Eq. (16d) and compute  $\Omega^{\tau+\Delta\tau}$  after assuming  $\Omega'' = 0$  at the bottom and top boundaries.
- 3) Advance  $\phi''$  and  $W''$  with Eqs. (16e) and (16c) and with boundary conditions (24) and (25).
- 4) Compute  $p''$  and  $\mu''$  with Eqs. (18) and (20).

After the acoustic update,  $p'$  and  $\alpha'$  are updated based on Eqs. (11) and (14f) to make sure they satisfy the equation of state and the hydrostatic relation at every RK step. Finally, after all RK steps, we conduct hydrostatic rebalancing, and then the model advances to the next time step.

## d. Model stability

We implemented the moving bottom in WRF version 3.8.1 with a third-order RK method (RK3) to integrate the model in time, a fifth-order spatial discretization for horizontal advection and a third-order spatial discretization for vertical advection. For time discretization, the RK3 method is third-order accurate only for linear equations, and second-order accurate for nonlinear equations (Skamarock et al. 2008). For spatial discretization, terms other than advection in the governing Eqs. (16a)–(16e) and (19a)–(19e) are discretized with a second-order central difference scheme. Therefore, the overall accuracy of WRF is second-order in both time and space. Model stability is dictated by the RK3 and the acoustic time step constraints. For 3D flows, the time step should satisfy

$$\Delta t < \frac{C_r \Delta x}{\sqrt{3} u_{\text{max}}}, \tag{35}$$

where  $C_r$  is the maximum CFL number (Skamarock et al. 2008). Theoretical  $C_r$  values for different temporal and spatial scheme combinations are documented in Wicker and Skamarock (2002), and the  $1/\sqrt{3}$  factor is to account for the fact that in practice the maximum CFL number should be less than the theoretical value  $C_r$ .

The acoustic time steps are integrated in an explicit forward scheme (except the semi-implicit scheme related to Eqs. (16c) and (16e) for  $0 \leq \beta < 1$ ), for which stability requires  $C_r = 1/2$

in practice (Skamarock et al. 2008). The acoustic time step is  $\Delta\tau = \Delta t/n_s$ , where  $n_s$  is the number of sound steps in each model time step, and the constraint  $\Delta\tau < \Delta x/(2c_s)$  gives

$$\Delta t < \frac{n_s \Delta x}{2 c_s}. \quad (36)$$

The smaller of (35) and (36) is the maximum time step limit of the model. The value of  $n_s$  can be set to maximize the efficiency of the computation. The acoustic step, Eqs. (16a) to (16e), are faster to advance than the RK step, Eqs. (14a) to (14e), because the right-hand sides of (16a) to (16e) reuse the values computed in the last RK step, and are not updated during every acoustic step. The trade-off is that the more acoustic steps, the longer it takes to advance each model step, while on the other hand, a larger  $n_s$  gives a larger limit for the model time step as indicated by Eq. (36). In fact, a simulation with  $n_s = 40$  is twice as fast as a simulation with  $n_s = 4$ . Nevertheless, care should be taken using large values of  $n_s$  with a moving bottom. If the bottom is stationary, then setting  $n_s = 40$  gives similar turbulent statistics as in  $n_s = 4$ , but if the bottom moves, sound waves will be enhanced and reflected in the computational domain with  $n_s = 40$ . The resulting Reynolds stress profile will show vertical oscillations with a wavelength of  $C_s \Delta t$ , which are not present in simulations with  $n_s \leq 4$ . This is likely due to the fact that when  $n_s$  is very large, the acoustic step Eqs. (16a) to (18) keep reusing the values of the last RK step while they are no longer a good estimate of the right-hand sides of (16a) to (18). When the bottom is stationary, the effect of this mismatch is small, but when the bottom moves, surface motions resonate with standing acoustic modes leading to errors. We found that using  $n_s = 4$  takes advantage of the acoustic substepping while eliminating the vertical oscillations.

### 3. Model validation

In this section, we present three test cases to validate the moving-wave implementation in WRF-LES: 1) inviscid laminar flow, 2) viscous laminar flow and 3) turbulent flow. For all three cases, the bottom boundary is prescribed as a monochromatic linear water wave. The wave propagates in the streamwise direction, here taken to be the  $x$  direction, and there is no variation in the spanwise ( $y$ ) direction. Cases 1 and 2 have analytical solutions of the airflow over moving waves, whereas case 3 does not have an analytical solution. Therefore, for case 3 we validate the code by comparing the moving-wave simulation results to an equivalent case in a wave-following reference frame, such that it can be simulated with the original fixed-bottom WRF-LES code that has already been extensively validated.

#### a. Inviscid flow over a linear water wave

For this test case, the height of the bottom boundary is given by the linear monochromatic water wave

$$h = a \sin(kx - \omega t), \quad (37)$$

where  $a$  is the wave amplitude,  $k = 2\pi/\lambda$  is the horizontal wavenumber associated with wavelength  $\lambda$ , and  $\omega$  is the wave

frequency, which is assumed to satisfy the deep-water dispersion relation  $\omega = \sqrt{gk}$ . In the limits of small steepness and amplitude, i.e.,  $ka \ll 1$  and  $a/H \ll 1$ , where  $H$  is the domain height, the motion of the air is given by solving the potential flow equations (Kundu et al. 2016), which gives the analytical solution for the airflow and pressure above the wave as

$$u = -a\omega \frac{\cosh[k(z-H)]}{\sinh(kH)} \sin(kx - \omega t), \quad (38a)$$

$$w = a\omega \frac{\sinh[k(z-H)]}{\sinh(kH)} \cos(kx - \omega t), \quad (38b)$$

$$p' = -\frac{\rho a \omega^2 \cosh[k(z-H)]}{k \sinh(kH)} \sin(kx - \omega t). \quad (38c)$$

To ensure linear dynamics as well as no flow separation in WRF, we set  $a = 0.08$  m and  $\lambda = 56.2$  m, giving steepness  $ka = 0.01$ , wave period  $T = 6$  s, and wave phase speed  $c = \sqrt{g/k} = 9.37$  m s<sup>-1</sup>. These settings are representative of a typical wave found in coastal seas. The computational domain is  $L = \lambda = 56.2$  m and  $H = 100$  m. Periodic boundary conditions are applied in the horizontal directions. WRF has several options to damp the vertical velocity near the top boundary, including a layer of increased diffusion, a Rayleigh relaxation layer and an implicit gravity wave damping layer. They are efficient to reduce acoustic and gravity wave reflection at the top of the domain but are not necessary for this test case. In fact, for all test cases in this paper, we use no damping on the top boundary, and apply free-shear boundary condition at the top. The flow is homogeneous in the spanwise direction, with uniform grid spacings  $\Delta x = \Delta y = 1.12$  m and  $\Delta z = 1$  m. The time step is  $\Delta t = 0.01$  s with  $n_s = 4$  acoustic steps.

As shown in Fig. 3, the  $x$ - $z$  contours of  $u$ ,  $w$ , and  $p'$  show good agreement between the simulation results and the analytical solutions. The moving-bottom WRF Model also reproduces the analytical vertical profiles of  $u$ ,  $w$ , and  $p'$  as shown in Fig. 4.

As an additional validation of the inviscid flow case, we use the original WRF-LES code to simulate inviscid flow over a fixed wavy bottom, but initialize the horizontal velocity with  $u = -c$  everywhere so that it is equivalent to the moving-wave case, except in a wave-following reference frame. We refer to this case as the moving-frame case, and the previous case with a moving wave as the fixed-frame case in the remainder of the paper. The moving-frame case uses the same computational domain and resolution as the fixed-frame case. We expect the results from the moving-frame case to be the same as the fixed-frame case after transforming the solutions to the same reference frame. To compare the results from the two cases, we assume that any transients in each solution have vanished, giving a steady solution for the moving-frame case and a time-periodic solution for the fixed-frame case. Then we note that the streamwise velocity in the steady solution of the moving-frame case,  $u_m(x, z)$ , is related to the streamwise velocity for the fixed-frame case,  $u_f(x, z, t)$ , with  $u_m(x, z) + c = u_f(x - ct, z, t)$ . Meanwhile,  $w_m(x, z) = w_f(x - ct, z, t)$  and  $p'_m(x, z) = p'_f(x - ct, z, t)$ . To ensure that the fixed-frame solution is aligned with the horizontal

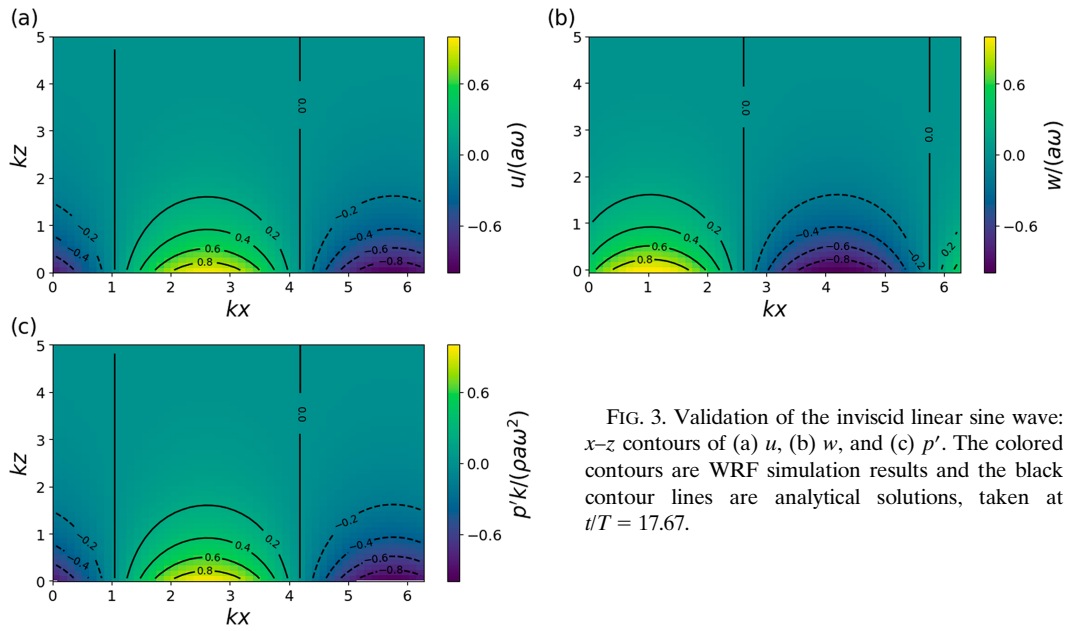


FIG. 3. Validation of the inviscid linear sine wave:  $x$ - $z$  contours of (a)  $u$ , (b)  $w$ , and (c)  $p'$ . The colored contours are WRF simulation results and the black contour lines are analytical solutions, taken at  $t/T = 17.67$ .

grid points associated with the moving-frame solution, we require  $x_m = x_f - ct + n\lambda$ , where  $n$  is an integer, and compare points at  $x = x_m$  in the moving-frame case with points at the corresponding location  $x = x_f$  in the fixed-frame case.

As shown in Fig. 5, the two cases agree with each other in terms of their vertical profiles of  $u$ ,  $w$ , and  $p'$ , and also match the analytical solutions. The overshoot of  $w$  in the fixed wave case at the top of the domain is likely due to acoustic wave

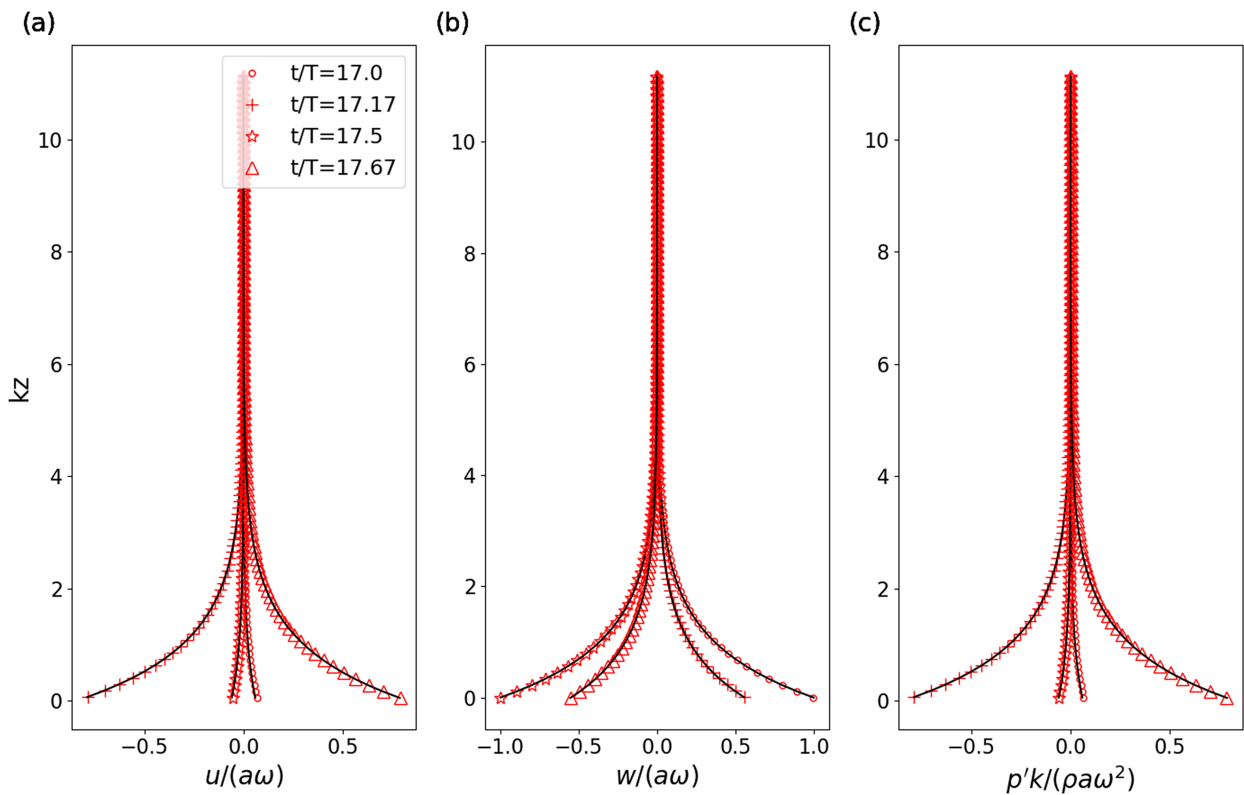


FIG. 4. Validation of the inviscid linear sine wave: vertical profiles of (a)  $u$ , (b)  $w$ , and (c)  $p'$ . The red symbols are WRF simulation results and the black lines are analytical solutions. Different symbols refer to different time instances.

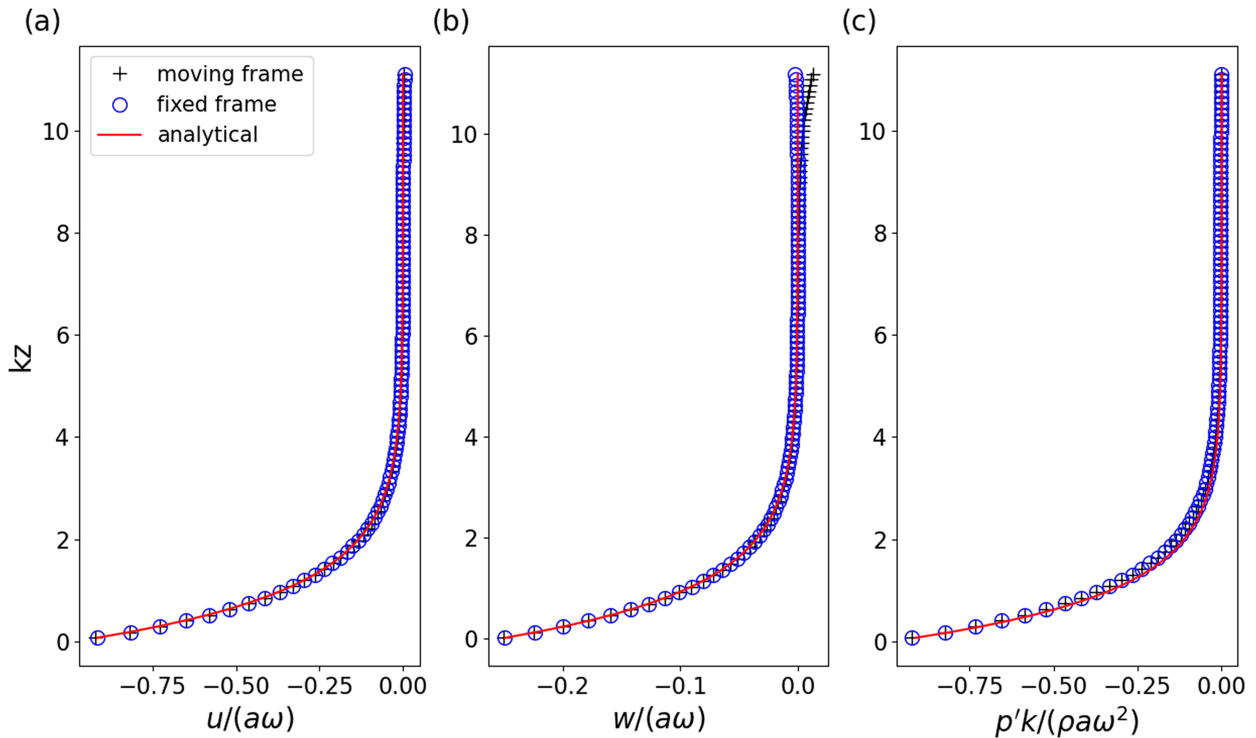


FIG. 5. Validation of the inviscid linear sine wave in different frames of reference: profiles of (a)  $u$ , (b)  $w$ , and (c)  $p'$  of the fixed-frame (blue circles) and the moving-frame simulations (black plus signs), along with the analytical solution (red lines), taken at  $t/T = 20$  and  $x = 0$  in the fixed reference frame.

reflection because there is no damping applied at the top boundary. Figure 5 shows an example of the vertical profile comparison taken at  $x = 0$  in the moving-frame case, although the same level of agreement is attained for other locations as well.

Having demonstrated that the method reproduces the linear inviscid theory, we now demonstrate the error convergence of the moving-bottom WRF code using an inviscid wave with  $a = 0.16$  m and  $\lambda = 100$  m. The domain size is  $L = 100$  m and  $H = 100$  m. For temporal convergence, a spatial resolution of  $\Delta x = 2.5$  m is used, and for spatial convergence, a temporal resolution of  $\Delta t = 0.0005$  s is used. The simulations run for one second. Figures 6 and 7 show relative errors of  $u$ ,  $w$ , and  $p'$  as a function of  $\Delta t$  and  $\Delta x$ , respectively. The relative error is defined as the absolute difference in  $u$ ,  $w$ , or  $p'$  between each case and the case with the next smaller  $\Delta t$  or  $\Delta x$ . Given a location in  $x$  (at the centerline in  $y$ ), we compute the relative error using three types of norms: the  $L_1$ ,  $L_2$ , and  $L_\infty$  norms computed with data over all grid points from  $\zeta = 0$  to 1. The convergence rates are sensitive to the error metric that is chosen, as shown in Figs. 6 and 7. The numerical values of the convergence rates are computed as the slopes of the lines in Figs. 6 and 7. They are listed in Table 1. Convergence rates indicated by the  $L_1$  and  $L_\infty$  norms are almost the same for  $u$  and  $w$ , but different for  $p'$ . For temporal convergence, errors using the  $L_2$  norm indicate roughly second-order accuracy for  $w$ , nearly third-order accuracy for  $u$ , and between first- and second-order accuracy for  $p'$ . The deviation from second-order accuracy for  $u$  and  $p'$  might be due to the fact that inviscid flow is sensitive to initial transients. For spatial

convergence, errors using the  $L_1$  and  $L_\infty$  norms indicate second-order accuracy, while errors using the  $L_2$  norm indicate roughly fourth-order accuracy. Although we do not have a clear explanation for the behavior of the different norms, we can find error metrics that display second-order accuracy for spatial convergence, consistent with the fact that WRF is second-order accurate in space as discussed in section 2d.

#### b. Viscous laminar flow over a linear wave

In this case, molecular viscosity is added to the flow. A Dirichlet boundary condition is applied at the bottom, and periodic boundary conditions are applied in the horizontal directions. The wave prescribed at the bottom is the same as Eq. (37). The linear analytical solutions for a viscous laminar flow over such a wave in a deep domain ( $kH \gg 1$ ) are given by the real parts of the complex solutions (Yang and Shen 2011b):

$$u = u_0 + u_v, \quad (39a)$$

$$w = w_0 + w_v, \quad (39b)$$

$$u_0 = aA_1 k e^{i(kx - \omega t)} e^{-kz}, \quad (39c)$$

$$u_v = -ikk_1 aA_2 e^{i(kx - \omega t)} e^{-kk_1 z}, \quad (39d)$$

$$w_0 = iakA_1 e^{i(kx - \omega t)} e^{-kz}, \quad (39e)$$

$$w_v = aA_2 k e^{i(kx - \omega t)} e^{-kk_1 z}, \quad (39f)$$

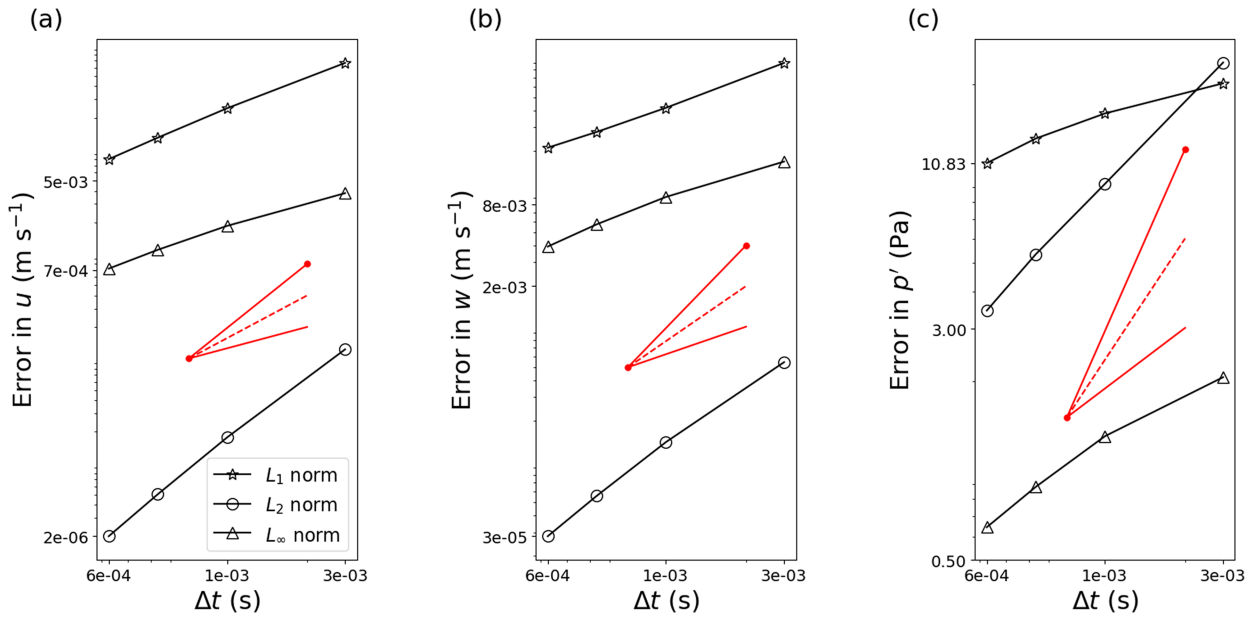


FIG. 6. Time-stepping error in (a)  $u$ , (b)  $w$ , and (c)  $p'$  relative to the results from the case with the next smaller  $\Delta t$  for the inviscid flow test case. The errors are computed with three types of norms:  $L_1$  norm (black stars),  $L_2$  norm (black circles), and  $L_\infty$  norm (black triangles). Lines indicate the following: first-order slope (red solid line), second-order slope (red dashed line), and third-order slope (red solid line with dots).

where  $\nu$  is the molecular viscosity of the air,  $u_0$  and  $w_0$  are the inviscid components of the solution [Eqs. (39c) and (39e)], while  $u_\nu$  and  $w_\nu$  are the viscous components of the solution [Eqs. (39d) and (39f)]. The coefficients  $k_1$ ,  $k_2$ ,  $A_1$ , and  $A_2$  are given by

$$k_1 = \sqrt{1 - \frac{i\omega}{k^2\nu}}, \quad (40a)$$

$$k_2 = \sqrt{1 - \frac{i\omega}{k^2\nu_w}}, \quad (40b)$$

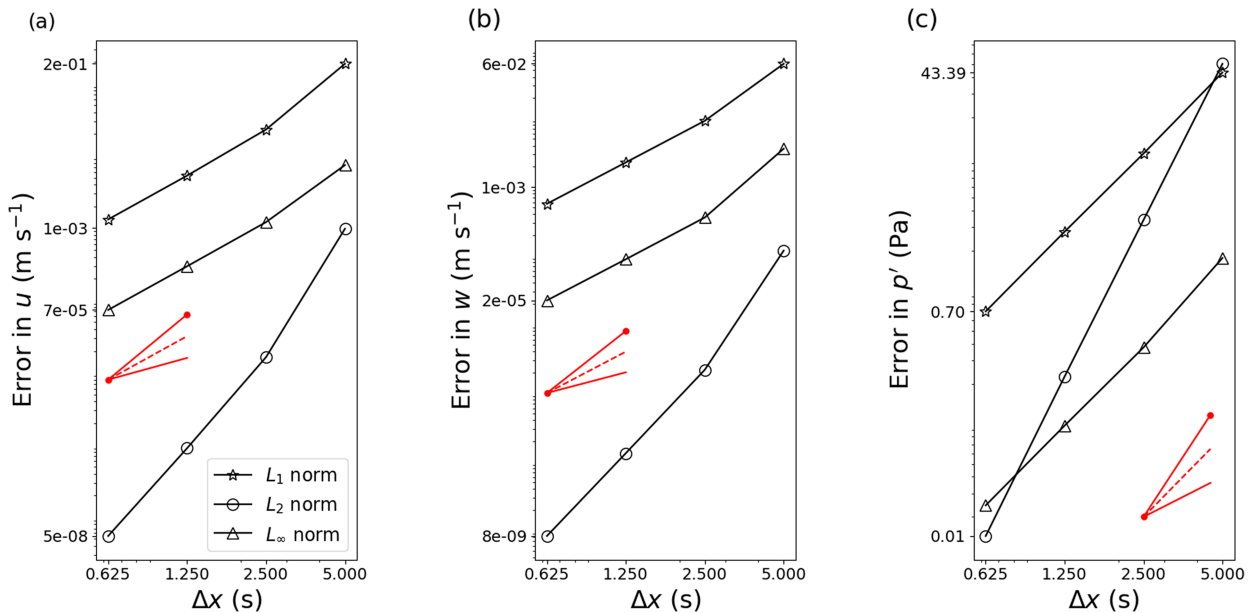


FIG. 7. Spatial discretization error in (a)  $u$ , (b)  $w$ , and (c)  $p'$  relative to the results from the case with the next smaller  $\Delta x$  for the inviscid flow test case. The errors are computed with three types of norms:  $L_1$  norm (black stars),  $L_2$  norm (black circles), and  $L_\infty$  norm (black triangles). Lines are as follows: first-order slope (red solid line), second-order slope (red dashed line), and third-order slope (red solid line with dots).

TABLE 1. Temporal and spatial convergence rates of the inviscid flow and the viscous laminar flow test cases for  $u$ ,  $w$ , and  $p'$  using  $L_1$ ,  $L_2$ , and  $L_\infty$  norms.

		Inviscid			Viscous laminar		
		$L_1$	$L_2$	$L_\infty$	$L_1$	$L_2$	$L_\infty$
$u$	Temporal	1.53	2.80	1.20	1.53	3.06	1.51
	Spatial	2.01	4.04	2.01	2.01	4.01	2.01
$w$	Temporal	1.10	2.14	1.05	1.12	2.52	1.45
	Spatial	2.00	4.01	1.99	2.00	3.99	1.99
$p'$	Temporal	0.45	1.39	0.84	1.04	2.21	1.29
	Spatial	1.99	3.98	1.99	2.03	4.05	2.02

$$A_1 = ic \frac{k_1 k_2 + k_2 + r_\rho r_\nu k_1^2 - 1 + k_1}{(k_2 + r_\rho r_\nu k_1 + r_\rho r_\nu + 1)(k_1 - 1)}, \quad (40c)$$

$$A_2 = 2c \frac{k_2 + r_\rho r_\nu}{(k_2 + r_\rho r_\nu k_1 + r_\rho r_\nu + 1)(k_1 - 1)}, \quad (40d)$$

where  $\nu_w$  is the molecular viscosity of water,  $r_\rho = \rho/\rho_w$  and  $r_\nu = \nu/\nu_w$  are the ratios of density and molecular viscosity between the air and the water, respectively. In this test case, we use  $r_\rho = 10^{-3}$ ,  $r_\nu = 10$ , and  $\nu$  is set to a value such that the Reynolds number  $Re = c/(k\nu) = 100$ . To resolve the Stokes boundary layer, which has thickness  $\delta = \sqrt{2\nu/\omega} = 1.3$  m,  $\Delta z = 0.1$  m at the bottom, and is stretched upward with a ratio of 1.05. The horizontal grid spacing is  $\Delta x = \Delta y = 1.12$  m. The wave amplitude,

wavelength and domain size are the same as the inviscid linear sine wave case discussed in section 3a.

Figures 8 and 9 show good agreement between WRF simulation results and the analytical solutions for the viscous laminar flow test case. In Fig. 8a, strong shear is present in  $u$  in the boundary layer ( $z < \delta$ ) due to the Stokes boundary layer. Above the boundary layer,  $u$  and  $w$  transition to the inviscid solutions. The error in  $u$  between the WRF simulation results and the analytical solution has a magnitude of  $0.05a\omega$ , which is 5% of the analytical solution (Fig. 9c). The error in  $w$  has a magnitude of up to only  $0.01a\omega$ , which is 1% of the analytical solution (Fig. 9d). The errors are concentrated in the height below  $5\delta$ , above which they approach zero. Figure 9 shows vertical profiles of the viscous velocities  $u_\nu$  and  $w_\nu$  in the boundary layer, which again agree well with the analytical solutions. Because the simulation results and the analytical solution for  $p'$  remain the same in the viscous and the inviscid flow cases, the results for  $p'$  are not shown here.

Using the same setup as the inviscid flow test case, discussed in section 3a, we show the temporal and spatial convergence of the viscous laminar flow case in Figs. 10 and 11. The numerical values of the convergence rates are computed as the slopes of the lines in Figs. 10 and 11. They are listed in Table 1. For temporal convergence (Fig. 10), errors using the  $L_2$  norm indicate roughly second-order accuracy for  $w$  and  $p'$ , and third-order accuracy for  $u$ . The  $L_1$  and  $L_\infty$  norms yield lower convergence rates that are between first- and second-order. For spatial convergence (Fig. 11), errors using the  $L_\infty$  and  $L_1$  norms are parallel to each other for all variables and

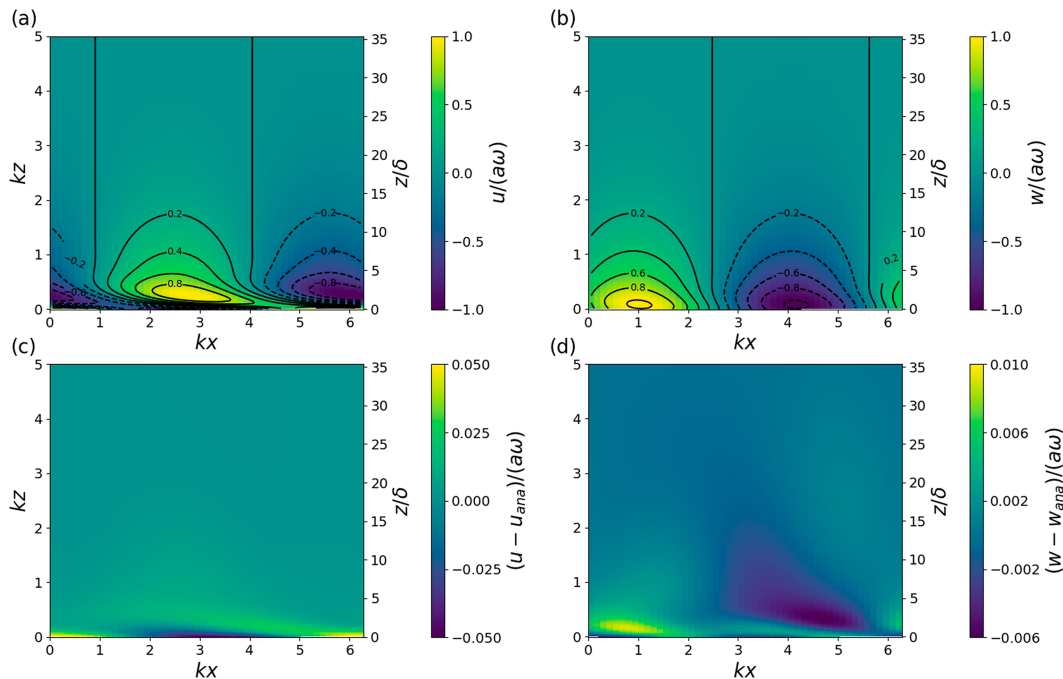


FIG. 8. The viscous linear sine wave case:  $x$ - $z$  contours of (a)  $u$ , (b)  $w$ , (c) the error in  $u$ , and (d) the error in  $w$  between the WRF simulation results and the analytical solution. The colored contours are WRF simulation results and the black contour lines are analytical solutions, taken at  $t/T = 17.67$ . The  $y$  axis on the right shows the height normalized by the Stokes boundary layer thickness  $\delta$ .

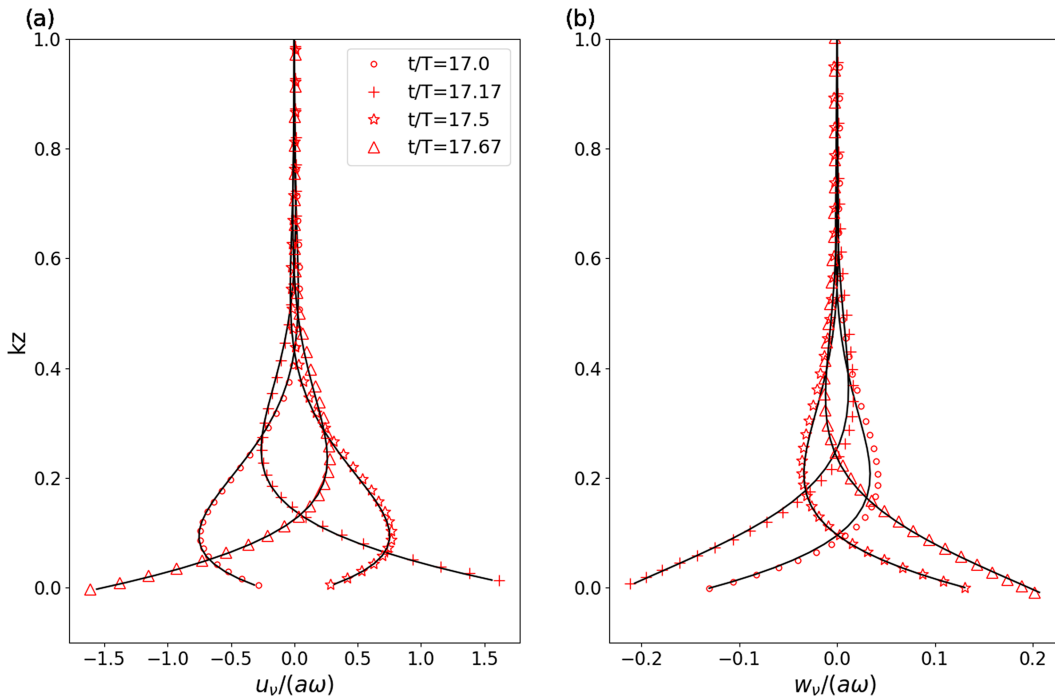


FIG. 9. The viscous linear sine wave case: vertical profiles of (a)  $u_v$  and (b)  $w_v$ . The red symbols are WRF simulation results, and the black lines are analytical solutions. Different symbols refer to different times.

indicate second-order accuracy, but errors using the  $L_2$  norm indicate fourth-order accuracy, similar to the inviscid case. Again, we do not have a clear explanation for the behaviors of the different norms, but at least one of the three error metrics show second- or higher-order convergence for both time

and space for the viscous laminar flow case. The spatial errors for the viscous laminar flow case form straighter lines (Fig. 11) than the spatial errors for the inviscid flow case (Fig. 7) and are slightly closer to the expected second-order slope. This is likely because of the smoothing effect of viscosity, which reduces

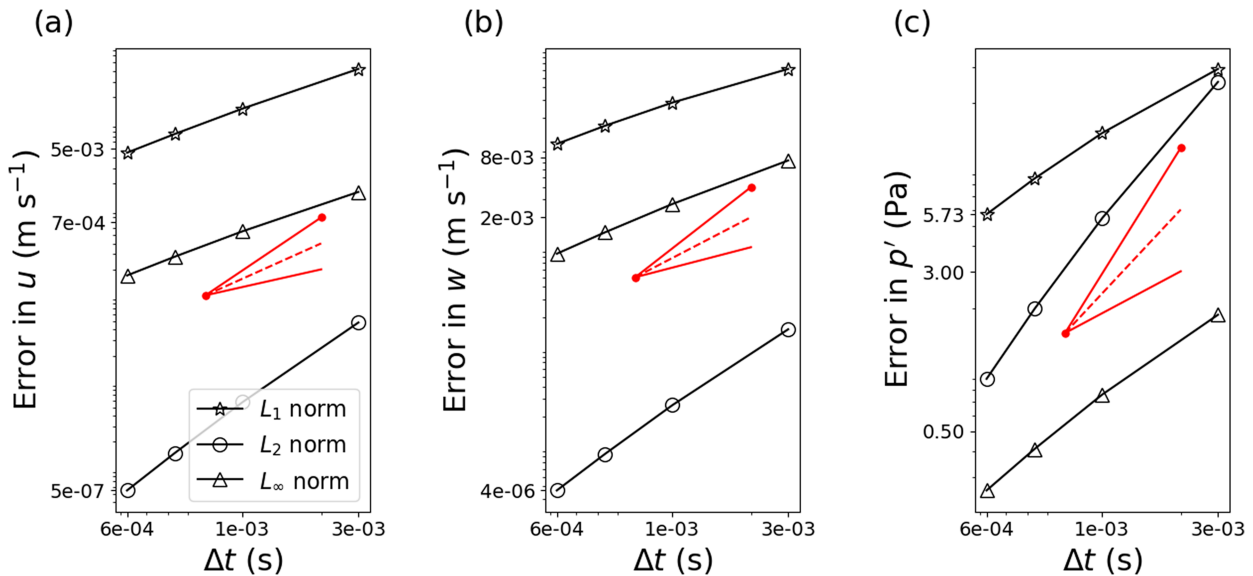


FIG. 10. Time-stepping error in (a)  $u$ , (b)  $w$ , and (c)  $p'$  relative to the results from the case with the next smaller  $\Delta t$  for the viscous laminar flow test case. The errors are computed with three types of norms:  $L_1$  norm (black stars),  $L_2$  norm (black circles), and  $L_\infty$  norm (black triangles). Lines are as follows: first-order slope (red solid line), second-order slope (red dashed line), and third-order slope (red solid line with dots).

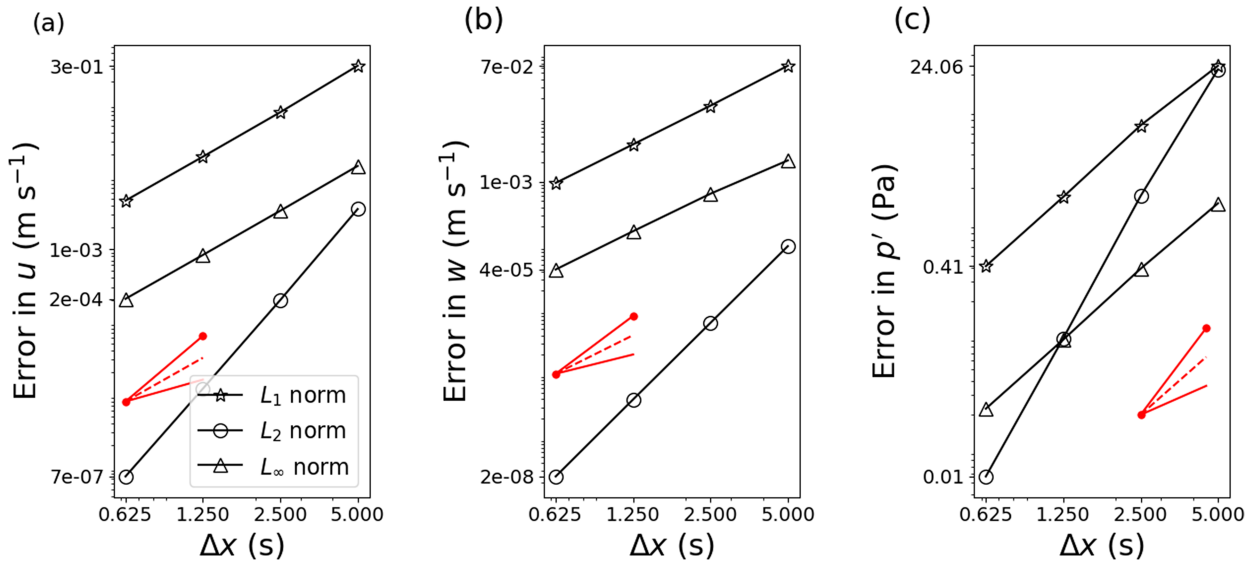


FIG. 11. Spatial discretization error in (a)  $u$ , (b)  $w$ , and (c)  $p'$  relative to the results from the case with the next smaller  $\Delta x$  for the viscous laminar flow test case. The errors are computed with three types of norms:  $L_1$  norm (black stars),  $L_2$  norm (black circles), and  $L_\infty$  norm (black triangles). Lines are as follows: first-order slope (red solid line), second-order slope (red dashed line), and third-order slope (red solid line with dots).

transients and grid-scale noise that are more likely to be present in the inviscid test case.

### c. Turbulent flow over a monochromatic wave

Here we test the moving-bottom WRF code with turbulent flow over a moving sine wave and analyze the mean momentum budget. The mean momentum budget in WRF can be derived from the streamwise momentum equation:

$$\begin{aligned} \frac{\partial U}{\partial \tau} + \frac{\partial(Uu)}{\partial \xi} + \frac{\partial(Vu)}{\partial \eta} + \frac{\partial(\Omega u)}{\partial \zeta} - \partial_\xi(p\phi_\zeta) + \partial_\zeta(p\phi_\xi) \\ = \mu F + \frac{\partial}{\partial \xi_k} \left( \mu \tau_{1j,\text{SGS}} \frac{\partial \xi_k}{\partial x_j} \right), \end{aligned} \quad (41)$$

where  $F = u_*^2/H$  is the pressure gradient force,  $\tau_{ij,\text{SGS}}$  is the subgrid scale (SGS) stress and  $(\xi_1, \xi_2, \xi_3) = (\xi, \eta, \zeta)$ . Using the transformation metrics in Eqs. (4a)–(4c) and  $J = \zeta_z = -\rho g/\mu$ , the SGS stress term can be written as

$$\frac{\partial}{\partial \xi_k} \left( \mu \tau_{1j,\text{SGS}} \frac{\partial \xi_k}{\partial x_j} \right) = \rho g \left( \tau_{13,\text{SGS}} - \tau_{11,\text{SGS}} \frac{\partial z}{\partial \xi} - \tau_{12,\text{SGS}} \frac{\partial z}{\partial \eta} \right). \quad (42)$$

For simplicity, we define

$$\tau_{\text{SGS}} = \tau_{13,\text{SGS}} - \tau_{11,\text{SGS}} \frac{\partial z}{\partial \xi} - \tau_{12,\text{SGS}} \frac{\partial z}{\partial \eta}. \quad (43)$$

Averaging Eq. (41) in time and horizontally makes the horizontal advection and the horizontal pressure gradient terms vanish due to horizontal periodicity. Then, vertical integration from the bottom ( $\zeta = 1$ ) to a certain height  $\zeta$  results in

$$\int_1^\zeta \frac{\partial}{\partial \zeta'} \langle \Omega u + p\phi_\xi - \rho g \tau_{\text{SGS}} \rangle d\zeta' = \int_1^\zeta \langle \mu \rangle F d\zeta',$$

which gives

$$\langle \Omega u + p\phi_\xi - \rho g \tau_{\text{SGS}} \rangle|_\zeta - \tau_w = \langle \mu \rangle F (\zeta - 1), \quad (44)$$

where  $\tau_w$  is the total stress at the bottom, and  $\langle \rangle$  represents the average in time and in the horizontal. At the top boundary  $\zeta = 0$ , the total stress  $\langle \Omega u + p\phi_\xi - \rho g \tau_{\text{SGS}} \rangle|_{\zeta=0}$  is zero, which requires

$$\tau_w = \langle \mu \rangle F. \quad (45)$$

The total stress at height  $\zeta$  is then given by

$$\tau_{\text{tot}} = \langle \Omega u + p\phi_\xi - \rho g \tau_{\text{SGS}} \rangle = \langle \mu \rangle F \zeta. \quad (46)$$

Since the flow in our applications is essentially incompressible and the vertical variation in density is negligible assuming a neutral atmosphere condition, we assume constant density  $\rho = \rho_0$ . To express the total stress as a function of  $z$  instead of  $\zeta$ , we use the definition of  $\zeta$  [Eq. (1)] and the hydrostatic relation  $\partial p/\partial z = -\rho_0 g$  to obtain

$$\begin{aligned} \zeta &= \frac{p_{h,s} - \int_0^z \rho_0 g dz' - \left( p_{h,s} - \int_0^H \rho_0 g dz' \right)}{p_{h,s} - \left( p_{h,s} - \int_0^H \rho_0 g dz' \right)} \\ &= 1 - \frac{z}{H}, \end{aligned} \quad (47)$$

which gives, after noting that  $\langle \mu \rangle = p_{h,s} = \rho_0 g H$ ,

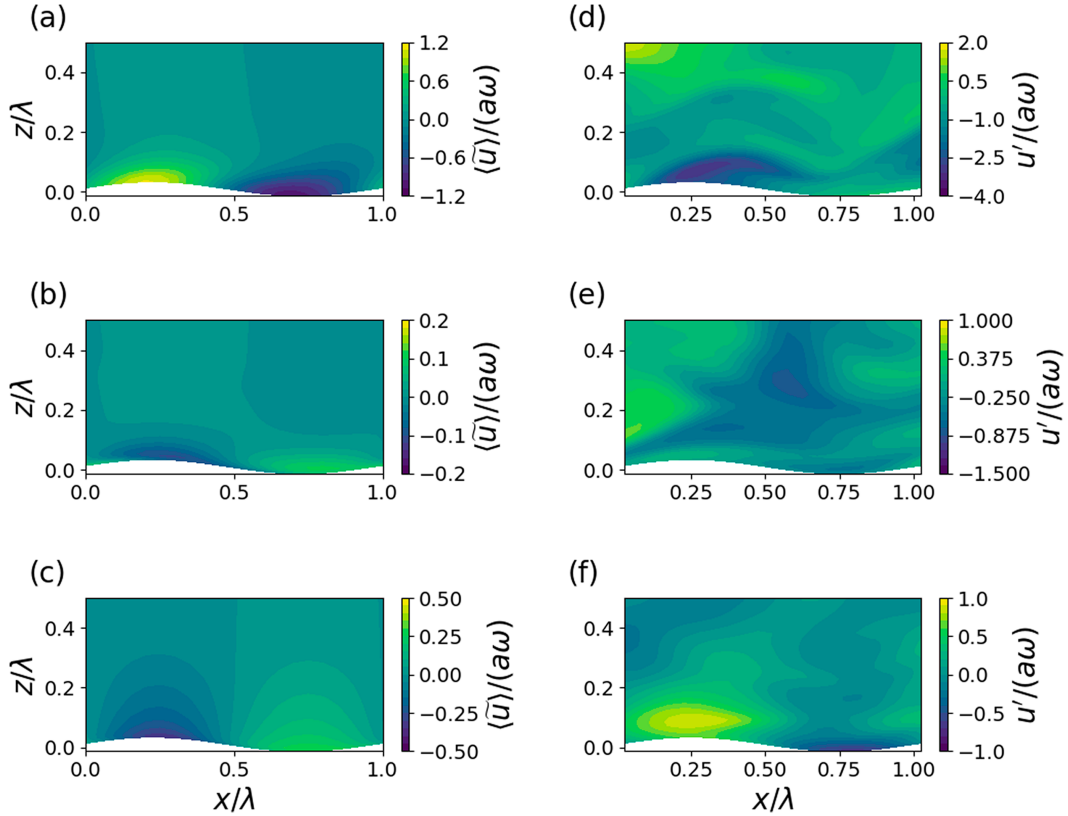


FIG. 12. Contours of (left) normalized wave-induced streamwise velocity  $\bar{u}$  and (right) instantaneous streamwise turbulent fluctuation  $u'$  taken after 95 eddy turnover periods along the channel center line ( $y = 75$  m) for the turbulent flow cases with wave age (a),(d)  $cu_* = 15$  (slow wave); (b),(e)  $cu_* = 28$  (intermediate wave); and (c),(f)  $cu_* = 50$  (fast wave).

$$\langle \Omega u + p\phi_\xi - \rho_0 g \tau_{\text{SGS}} \rangle = \rho_0 g u_*^2 \left(1 - \frac{z}{H}\right). \quad (48)$$

With Eq. (6) and  $J = -\rho_0 g/\mu$ ,  $\Omega$  can be rewritten as

$$\begin{aligned} \Omega &= J \left( W_n - \mu \frac{\partial z}{\partial \tau} \right) \\ &= -\rho_0 g \left( w - u \frac{\partial z}{\partial \xi} - v \frac{\partial z}{\partial \eta} - \frac{\partial z}{\partial \tau} \right) \\ &= -\rho_0 g \left( U_3 - \frac{\partial z}{\partial \tau} \right), \end{aligned} \quad (49)$$

where  $U_3 = w - u(\partial z/\partial \xi) - v(\partial z/\partial \eta)$  is the contravariant velocity normal to the  $\zeta$  surfaces for incompressible flow. Dividing both sides of Eq. (48) by  $-\rho_0 g$  then gives

$$-\left\langle \left( U_3 - \frac{\partial z}{\partial \tau} \right) u - \frac{p}{\rho_0} \frac{\partial z}{\partial \xi} + \tau_{\text{SGS}} \right\rangle = u_*^2 \left(1 - \frac{z}{H}\right). \quad (50)$$

To analyze the turbulence statistics, a triple decomposition is used following Hussain and Reynolds (1970). For a physical quantity  $f$ , we define

$$f = \bar{f}(\xi, \zeta) + f'(\xi, \eta, \zeta, t) = \langle f \rangle(\xi, \zeta) + \tilde{f}(\xi, \zeta) + f'(\xi, \eta, \zeta, t), \quad (51)$$

where  $\bar{f}$  is the phase average,  $\langle f \rangle$  is the average over time and the horizontal,  $\tilde{f}$  is the wave-induced fluctuation, and  $f'$  is the turbulent fluctuation. To compute the phase average  $\bar{f}$ , we first apply the Fourier transform to  $f$  in the direction of  $\xi$ , and then shift it to zero-phase in Fourier space, followed by an inverse Fourier transform to map it back to physical space. In general, a quantity with phase  $ct$ , i.e.,  $f(x - ct)$ , can be represented by  $e^{-2\pi i k c t} \hat{f}(k)$ , where  $\hat{f}(k)$  is the Fourier coefficient of  $f(x)$  associated with wavenumber  $k$ . Therefore, the phase shifting of  $f(x - a)$  is accomplished by multiplying its Fourier coefficients by  $e^{2\pi i k c t}$ , and then applying an inverse Fourier transform. Mathematically, this is represented by

$$\bar{f}(\xi, \zeta) = \frac{1}{(t_2 - t_1)D} \int_{t_1}^{t_2} \int_0^D \mathcal{F}^{-1} \{ e^{2\pi i k c t} \mathcal{F}[f(\xi, \eta, \zeta, \tau)] \} d\eta d\tau, \quad (52)$$

where  $\mathcal{F}$  and  $\mathcal{F}^{-1}$  denote the Fourier transform and its inverse,  $D$  is the width of the computational domain, and  $[t_1, t_2]$  is the time window for averaging. The mean value and the wave-induced fluctuation are then computed with

$$\langle f \rangle(\xi, \zeta) = \frac{1}{L} \int_0^L \bar{f}(\xi, \zeta) d\xi, \quad (53a)$$

$$\tilde{f}(\xi, \zeta) = \bar{f}(\xi, \zeta) - \langle f \rangle(\xi, \zeta). \quad (53b)$$

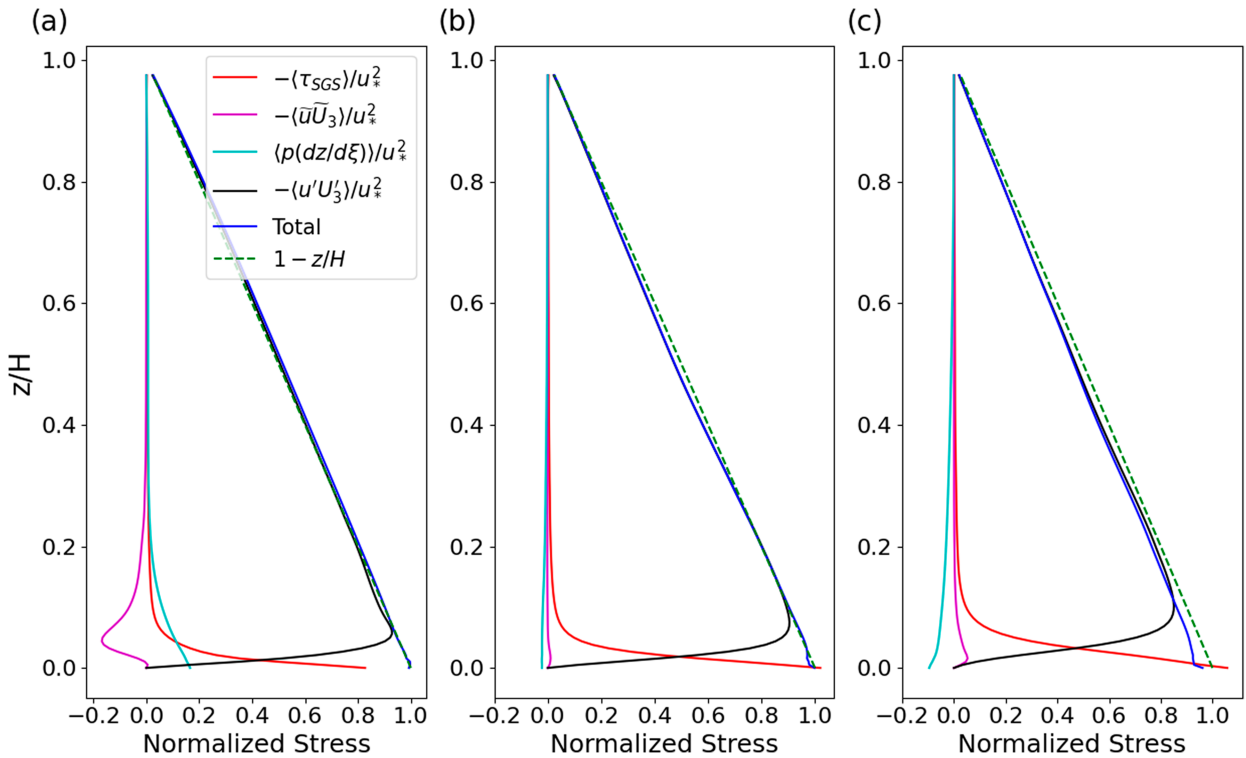


FIG. 13. Stress profiles of turbulent flow over a moving sine wave with wave age (a)  $clu_* = 15$ , (b)  $clu_* = 28$ , and (c)  $clu_* = 50$ .

To separate out wave-induced effects, the mean momentum budget needs to be analyzed in a wave-following frame, in which the horizontal velocity  $u$  is translated by the wave phase speed  $c$  and  $\partial z/\partial \tau$  vanishes (Hara and Sullivan 2015). With the triple decomposition applied to the velocities, Eq. (50) is given by

$$-\langle u'W' \rangle - \langle \tilde{u}\tilde{U}_3 \rangle + \left\langle \frac{p}{\rho_0} \frac{\partial z}{\partial \xi} \right\rangle - \langle \tau_{\text{SGS}} \rangle = u_*^2 \left( 1 - \frac{z}{H} \right). \quad (54)$$

The terms on the left-hand side are, in order from left to right, the turbulent stress, the wave-induced stress, the pressure stress, and SGS stress. At  $z = h$ , the pressure stress is the form drag.

In the turbulent flow test case, the wave height has the same form as Eq. (37), with  $a = 0.8$  m and  $\lambda = 50$  m, which results in a steepness of  $ka = 0.1$ . The computational domain is  $300 \text{ m} \times 150 \text{ m} \times 100 \text{ m}$ , with  $120 \times 60 \times 80$  grid points in the streamwise ( $x$ ), spanwise ( $y$ ) and vertical ( $z$ ) directions. The horizontal grid spacing is  $\Delta x = \Delta y = 2.5$  m. The vertical grid spacing is  $\Delta z = 0.5$  m at the lowest level above the wave surface, and is continuously stretched by a factor of 1.02 from one grid cell to the next to the top of the domain. The time step size is  $\Delta t = 0.01$  s, with  $n_s = 4$ . The Smagorinsky closure scheme is used to compute the turbulent eddy-viscosity. The flow is driven by a constant pressure gradient forcing, which is set to achieve a desired wave age  $c/u_*$ , i.e., the friction velocity  $u_*$  varies with the prescribed pressure gradient forcing while the wave phase speed  $c$  is fixed. We ran simulations with three different wave ages, which are categorized as a slow

wave ( $c/u_* = 15$ ), an intermediate wave ( $c/u_* = 28$ ) and a fast wave ( $c/u_* = 50$ ). The simulations are run for approximately 60 eddy turnover periods, and then an additional 35–40 eddy turnover periods to compute the statistics.

The presence of surface waves has a notable effect on altering the turbulence structure of the airflow, as previously reported in numerical simulations (e.g., Sullivan et al. 2000; Yang and Shen 2009), as well as laboratory experiments (e.g., Cheung and Street 1988; Buckley and Veron 2016). Here, we present results of WRF simulations on the wave-induced turbulence quantities in the wind. Figure 12 shows contours of the wave-induced streamwise velocity  $\tilde{u}$  and the turbulent fluctuation of the streamwise velocity  $u'$  within one wavelength above the surface. The slow wave induces the highest magnitudes of  $\tilde{u}$  and  $u'$  (Figs. 12a,d) while the intermediate wave induces the smallest magnitudes of  $\tilde{u}$  (Figs. 12b). In the slow wave case,  $\tilde{u}$  is nearly in-phase with the wave elevation (Fig. 12a), i.e., positive at the wave crest and negative at the wave trough. This is consistent with the fact that the wind accelerates when it travels through a contraction. In the intermediate wave case, the magnitude of  $\tilde{u}$  is only one-sixth of that in the slow wave case, and the influence of the wave extends to just  $0.1\lambda$  above the surface (Fig. 12b). In the fast wave case,  $\tilde{u}$  is out of phase with the wave elevation and the influence of the wave extends furthest among the three wave ages, i.e., roughly  $0.4\lambda$  above the surface (Fig. 12c). This can be explained by the fact that the wave moves faster than the wind near the bottom, i.e., the wind is moving from right to left relative to the wave, and thus has the opposite pattern in

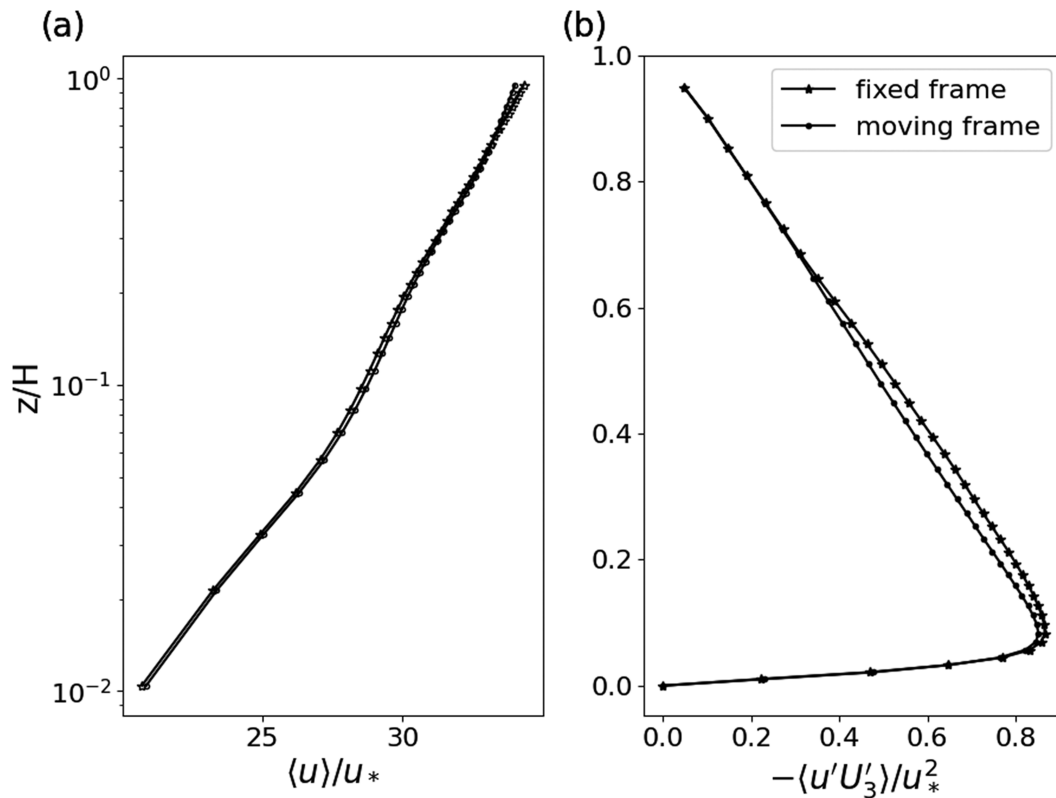


FIG. 14. Normalized mean streamwise velocity and Reynolds stress profiles for the fixed- and moving-frame cases of turbulent flow with  $c/u_* = 28$ .

$\bar{u}$  when compared to the slow wave case, where the wind is moving from left to right relative to the wave. As expected,  $u'$  is random and does not exhibit a regular pattern over different wave phases in all three cases (Figs. 12d–f).

Figure 13 shows the stress profiles for the turbulent flow cases with the three different wave ages. The intermediate wave generates near zero wave stress and form drag, while decreasing the wave age leads to much stronger wave stress and form drag. The magnitudes of the wave stress and form drag are consistent with the small magnitude of  $\bar{u}$  and  $u'$  for the intermediate wave and larger magnitudes of  $\bar{u}$  and  $u'$  for both the slow and fast waves (Fig. 12). The wave stress reaches a magnitude of 20% of the total stress for the slow wave (Fig. 13a), and about 5% for the fast wave (Fig. 13c). The pressure stress also reaches 20% of the total stress for the slow wave, and 10% for the fast wave, with opposite signs. Because the pressure stress displayed in Fig. 13 is on the left-hand side of Eq. (50), a positive (negative) pressure stress means a negative (positive) forcing by the waves on the wind, consistent with the fact that in the slow wave case, the wave propagates slower than the wind and consequently imposes a negative form drag on the wind, whereas in the fast wave case, the wave propagates faster than the wind and imposes a positive form drag. The normalized total stress agrees well with the linear theoretical profile for channel flows, with the fast wave case having a discrepancy of less than 5%.

To further validate our methodology, we compare the turbulent flow results with a moving wave in a fixed frame to a moving-frame case with a fixed wavy bottom. Details of the fixed- and moving-frame cases are discussed in section 3a. For the moving-frame case, the relative velocity  $u_r = u - c - u_w$  is used to transform the fixed frame to the moving frame, and then used to compute the bottom stress in Eqs. (28a) and (28b). The moving-frame case has the same numerical setup as the fixed-frame case. Figure 14 presents the results for  $c/u_* = 28$ . Both the mean velocity and Reynolds stress profiles agree well between the fixed- and moving-frame cases. Because the original WRF–LES code with a fixed-bottom has been extensively validated (Mirocha et al. 2010; Moeng et al. 2007; Bou-Zeid et al. 2005; Talbot et al. 2012; Di Bernardino et al. 2022), the agreement between the results from the case with a moving wave and an equivalent fixed-wave case validates our moving bottom model.

We also compare the wave growth rate with results from the literature. The wave growth rate  $\beta_g$  is defined as (Li et al. 2000)

$$\beta_g = \frac{2F_p}{(ak)^2}, \tag{55}$$

where  $F_p$  is the normalized form drag:

$$F_p = \frac{1}{\lambda u_*^2} \int_0^\lambda \frac{1}{\rho} \bar{p}|_{\zeta=1} \frac{\partial \bar{h}}{\partial x} dx. \tag{56}$$

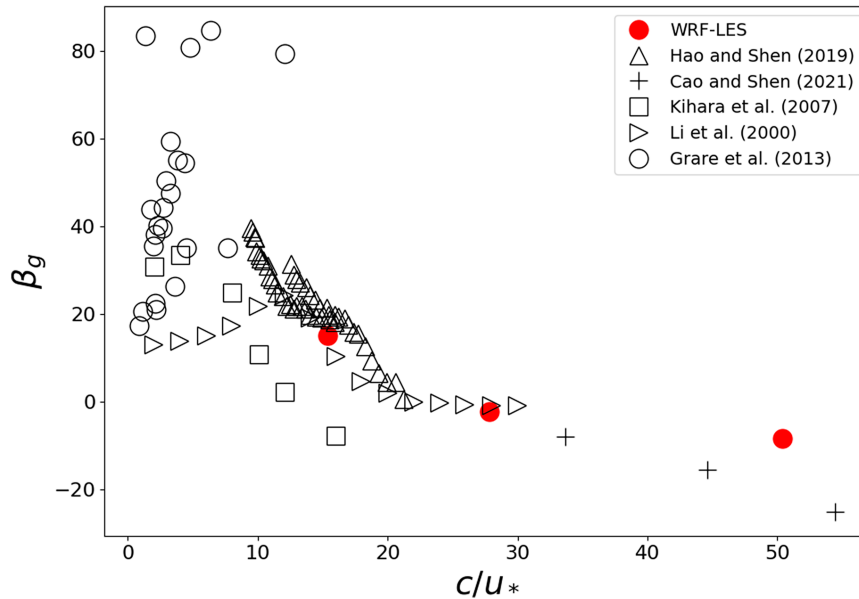


FIG. 15. Wave growth rate at different wave ages. Red circles show WRF-LES results, black triangles show wall-modeled LES results from Hao and Shen (2019), plus signs are wall-resolved LES from Cao and Shen (2021), black squares are DNS results from Kihara et al. (2007), black right triangles are Reynolds-averaged Navier-Stokes (RANS) results from Li et al. (2000), and black circles are experimental data from Grare et al. (2013).

As shown in Fig. 15,  $\beta_g$  is large for the slow wave, near zero for the intermediate wave, and regains its magnitude but with an opposite sign for the fast wave. This trend agrees with results from the literature, including the simulation results from Hao and Shen (2019) that used a wall-modeled, two-way coupled code and from Li et al. (2000) that used a Reynolds-averaged Navier-Stokes (RANS) model. At a wave age as high as 50, no data from wall-modeled LES simulations are available. Using a wall-resolved LES code, Cao and Shen (2021) reported a wave growth rate about twice as large as the result from WRF at a wave age of 50, but the former has 3-times-finer horizontal resolution and nearly 4-times-finer vertical resolution near the wave surface. The discrepancy is probably due to the use of a wall model in WRF to compute the wall shear stress versus directly resolving the wall shear stress, as well as a much lower grid resolution in WRF. Moreover, Cao and Shen (2021) did not report directly the wave growth rate for a case with  $c/u_* = 15.38$ , but it can be inferred from the corresponding pressure stress profile that  $\beta_g$  is approximately zero. In comparison, values of  $\beta_g$  at the same wave age obtained from the results of WRF and the wall-modeled LES in Hao and Shen (2019) are approximately 20, whereas DNS results in Kihara et al. (2007) suggest a value of around  $-10$ . This suggests that for smaller wave ages, wall-modeled LES predicts a higher wave growth rate than DNS. A comprehensive comparison between wall-modeled LES and wall-resolved LES regarding their predictions of wave growth rate requires further systematic study. Overall, the WRF simulations using the present moving bottom implementation reasonably capture the variation in wave growth rate as a function of wave

age. Furthermore, the wall-modeled WRF-LES is computationally efficient and allows for a larger domain extent to study, for example, the influence of wind power at wind turbine hub heights.

Although the explicit acoustic substepping algorithm in WRF requires a small model time step due to the fast sound speed, for our grid spacing we are able to use a time step of  $\Delta t = 0.01$  s with  $n_s = 4$ , as discussed in section 2d. For the slow wave case with  $c/u_* = 15$ , the eddy turnover period is 174 s, and it takes roughly 48 wall-clock hours to run 100 eddy turnover periods. For the fast wave case with  $c/u_* = 50$ , the eddy turnover period is 571 s, and it takes 6.3 wall-clock days to run 100 eddy turnover periods. The computational cost for the intermediate wave case is in between the other two cases. Given the  $120 \times 60 \times 80$  grid size, all turbulent cases use 192 processors located on 6 computational nodes. Therefore, despite the disadvantage of the CFL constraint on the model time step size, WRF-LES can efficiently simulate wind over moving waves and resolve scales relevant to LES.

#### 4. Conclusions

In this study, we presented the implementation of a moving bottom in WRF-LES and validated our code with idealized test cases that have analytical solutions, including flow over a monochromatic wave with and without viscosity. The results showed very good agreement with analytical solutions for a monochromatic linear sine wave. Next, we presented test cases of turbulent flow over a moving sine wave at three different wave ages. The stress profiles showed expected decomposition between Reynolds stress, SGS stress, wave stress and

pressure stress, and the total stress agrees with the theoretical profile for a pressure-driven channel flow. As further evidence for validation, we also compared the moving-wave cases with physically equivalent cases from the original WRF-LES code. In the former, the wave propagates in the downwind direction, while in the latter the wave does not propagate, but the wind is adjusted so that the wind relative to the waves is the same as in the former. Results indicate that the mean streamwise velocity and Reynolds stress profiles for the two cases match. Additionally, we found that the results from WRF successfully capture the trend of wave growth rate as a function of wave age found in the literature.

In the future, this moving bottom implementation will make WRF a powerful tool to study wind-wave interactions. Moisture and temperature stratification are not considered in this paper, but as existing features in WRF they can be easily incorporated into moving bottom simulations. This paper focuses on idealized wave and wind conditions for the purpose of validation. As future work, the method can be extended to more realistic conditions such as simulating wind over seas or combined seas and swell, or assimilating measured meteorological data as forcing conditions. With the ability of WRF to incorporate realistic meteorological conditions, a more comprehensive understanding of the influence of waves on the ABL can be achieved. This implementation will also enable WRF to be coupled with wave models like HOS, and eventually be extended to simulate wind-wave interactions under realistic conditions, contributing to scientific and engineering applications from wave effect parameterizations to offshore wind resource assessment.

*Acknowledgments.* This work was performed under the auspices of the U.S. Department of Energy by Lawrence Livermore National Laboratory under Contract DE-AC52-07NA27344, and supported by the Wind Energy Technologies Office. Support was also provided by the Office of Naval Research Grant N00014-20-1-2707. We thank Dr. Peter P. Sullivan at the National Center for Atmospheric Research for his extensive help and insight.

*Data availability statement.* All data and code used in this study will be available upon request.

## REFERENCES

- Aiyer, A. K., L. Deike, and M. E. Mueller, 2023: A sea surface-based drag model for large-eddy simulation of wind-wave interaction. *J. Atmos. Sci.*, **80**, 49–62, <https://doi.org/10.1175/JAS-D-21-0329.1>.
- Bou-Zeid, E., C. Meneveau, and M. Parlange, 2005: A scale-dependent Lagrangian dynamic model for large eddy simulation of complex turbulent flows. *Phys. Fluids*, **17**, 025105, <https://doi.org/10.1063/1.1839152>.
- Buckley, M. P., and F. Veron, 2016: Structure of the airflow above surface waves. *J. Phys. Oceanogr.*, **46**, 1377–1397, <https://doi.org/10.1175/JPO-D-15-0135.1>.
- Campbell, B. K., K. Hendrickson, and Y. Liu, 2016: Nonlinear coupling of interfacial instabilities with resonant wave interactions in horizontal two-fluid plane Couette–Poiseuille flows: Numerical and physical observations. *J. Fluid Mech.*, **809**, 438–479, <https://doi.org/10.1017/jfm.2016.636>.
- Cao, T., and L. Shen, 2021: A numerical and theoretical study of wind over fast-propagating water waves. *J. Fluid Mech.*, **919**, A38, <https://doi.org/10.1017/jfm.2021.416>.
- , B.-Q. Deng, and L. Shen, 2020: A simulation-based mechanistic study of turbulent wind blowing over opposing water waves. *J. Fluid Mech.*, **901**, A27, <https://doi.org/10.1017/jfm.2020.591>.
- , X. Liu, X. Xu, and B. Deng, 2023: Investigation on mechanisms of fast opposing water waves influencing overlying wind using simulation and theoretical models. *Phys. Fluids*, **35**, 015148, <https://doi.org/10.1063/5.0132131>.
- Castorrini, A., S. Gentile, E. Gerdali, and A. Bonfiglioli, 2023: Investigations on offshore wind turbine inflow modelling using numerical weather prediction coupled with local-scale computational fluid dynamics. *Renewable Sustainable Energy Rev.*, **171**, 113008, <https://doi.org/10.1016/j.rser.2022.113008>.
- Cheung, T. K., and R. L. Street, 1988: The turbulent layer in the water at an air–water interface. *J. Fluid Mech.*, **194**, 133–151, <https://doi.org/10.1017/S0022112088002927>.
- Cimarelli, A., F. Romoli, and E. Stalio, 2023: On wind-wave interaction phenomena at low Reynolds numbers. *J. Fluid Mech.*, **956**, A13, <https://doi.org/10.1017/jfm.2023.4>.
- D’Asaro, E., and C. McNeil, 2007: Air–sea gas exchange at extreme wind speeds measured by autonomous oceanographic floats. *J. Mar. Syst.*, **66**, 92–109, <https://doi.org/10.1016/j.jmarsys.2006.06.007>.
- Deskos, G., S. Ananthan, and M. A. Sprague, 2022: Direct numerical simulations of turbulent flow over misaligned traveling waves. *Int. J. Heat Fluid Flow*, **97**, 109029, <https://doi.org/10.1016/j.ijheatfluidflow.2022.109029>.
- Di Bernardino, A., V. Mazarella, M. Pecci, G. Casasanta, M. Cacciani, and R. Ferretti, 2022: Interaction of the sea breeze with the urban area of Rome: WRF mesoscale and WRF large-eddy simulations compared to ground-based observations. *Bound.-Layer Meteor.*, **185**, 333–363, <https://doi.org/10.1007/s10546-022-00734-5>.
- Dommermuth, D. G., and D. K. P. Yue, 1987: A high-order spectral method for the study of nonlinear gravity waves. *J. Fluid Mech.*, **184**, 267–288, <https://doi.org/10.1017/S002211208700288X>.
- Druzhinin, O., Y. Troitskaya, W.-T. Tsai, and P.-C. Chen, 2019: The study of a turbulent air flow over capillary-gravity water surface waves by direct numerical simulation. *Ocean Model.*, **140**, 101407, <https://doi.org/10.1016/j.ocemod.2019.101407>.
- Grare, L., W. L. Peirson, H. Branger, J. W. Walker, J.-P. Giovanangeli, and V. Makin, 2013: Growth and dissipation of wind-forced, deep-water waves. *J. Fluid Mech.*, **722**, 5–50, <https://doi.org/10.1017/jfm.2013.88>.
- Hao, X., and L. Shen, 2019: Wind-wave coupling study using LES of wind and phase-resolved simulation of nonlinear waves. *J. Fluid Mech.*, **874**, 391–425, <https://doi.org/10.1017/jfm.2019.444>.
- , T. Cao, Z. Yang, T. Li, and L. Shen, 2018: Simulation-based study of wind-wave interaction. *Procedia IUTAM*, **26**, 162–173, <https://doi.org/10.1016/j.piutam.2018.03.016>.
- Hara, T., and P. P. Sullivan, 2015: Wave boundary layer turbulence over surface waves in a strongly forced condition. *J. Phys. Oceanogr.*, **45**, 868–883, <https://doi.org/10.1175/JPO-D-14-0116.1>.

- Husain, N. T., T. Hara, and P. P. Sullivan, 2022a: Wind turbulence over misaligned surface waves and air–sea momentum flux. Part I: Waves following and opposing wind. *J. Phys. Oceanogr.*, **52**, 119–139, <https://doi.org/10.1175/JPO-D-21-00443.1>.
- , —, and —, 2022b: Wind turbulence over misaligned surface waves and air–sea momentum flux. Part II: Waves in oblique wind. *J. Phys. Oceanogr.*, **52**, 141–159, <https://doi.org/10.1175/JPO-D-21-00444.1>.
- Hussain, A. K. M. F., and W. C. Reynolds, 1970: The mechanics of an organized wave in turbulent shear flow. *J. Fluid Mech.*, **41**, 241–258, <https://doi.org/10.1017/S0022112070000605>.
- Kihara, N., H. Hanazaki, T. Mizuya, and H. Ueda, 2007: Relationship between airflow at the critical height and momentum transfer to the traveling waves. *Phys. Fluids*, **19**, 015102, <https://doi.org/10.1063/1.2409736>.
- Komori, S., R. Kurose, K. Iwano, T. Ukai, and N. Suzuki, 2010: Direct numerical simulation of wind-driven turbulence and scalar transfer at sheared gas–liquid interfaces. *J. Turbul.*, **11**, N32, <https://doi.org/10.1080/14685248.2010.499128>.
- Kumar, K., S. K. Singh, and L. Shemer, 2022: Directional characteristics of spatially evolving young waves under steady wind. *Phys. Rev. Fluids*, **7**, 014801, <https://doi.org/10.1103/PhysRevFluids.7.014801>.
- Kundu, P. K., I. M. Cohen, D. R. Dowling, and G. Tryggvason, 2016: *Fluid Mechanics*. 6th ed. Academic Press, 1002 pp.
- Large, W. G., J. C. McWilliams, and S. C. Doney, 1994: Oceanic vertical mixing: A review and a model with a nonlocal boundary layer parameterization. *Rev. Geophys.*, **32**, 363–403, <https://doi.org/10.1029/94RG01872>.
- Li, P. Y., D. Xu, and P. A. Taylor, 2000: Numerical modelling of turbulent airflow over water waves. *Bound.-Layer Meteor.*, **95**, 397–425, <https://doi.org/10.1023/A:1002677312259>.
- Li, T., and L. Shen, 2022a: Evolution of wave characteristics during wind-wave generation. *Proc. 34th Symp. on Naval Hydrodynamics*, Washington, DC, ONRS, 11 pp., <https://arxiv.org/pdf/2208.02489.pdf>.
- , and —, 2022b: The principal stage in wind-wave generation. *J. Fluid Mech.*, **934**, A41, <https://doi.org/10.1017/jfm.2021.1153>.
- Lin, M.-Y., C.-H. Moeng, W.-T. Tsai, P. P. Sullivan, and S. E. Belcher, 2008: Direct numerical simulation of wind-wave generation processes. *J. Fluid Mech.*, **616**, 1–30, <https://doi.org/10.1017/S0022112008004060>.
- Liu, S., A. Kermani, L. Shen, and D. K. P. Yue, 2009: Investigation of coupled air-water turbulent boundary layers using direct numerical simulations. *Phys. Fluids*, **21**, 062108, <https://doi.org/10.1063/1.3156013>.
- Mirocha, J. D., J. K. Lundquist, and B. Kosović, 2010: Implementation of a nonlinear subfilter turbulence stress model for large-eddy simulation in the advanced research WRF Model. *Mon. Wea. Rev.*, **138**, 4212–4228, <https://doi.org/10.1175/2010MWR3286.1>.
- Moeng, C.-H., J. Dudhia, J. Klemp, and P. Sullivan, 2007: Examining two-way grid nesting for large eddy simulation of the PBL using the WRF Model. *Mon. Wea. Rev.*, **135**, 2295–2311, <https://doi.org/10.1175/MWR3406.1>.
- Patton, E. G., P. P. Sullivan, B. Kosović, J. Dudhia, L. Mahrt, M. Žagar, and T. Marić, 2019: On the influence of swell propagation angle on surface drag. *J. Appl. Meteor. Climatol.*, **58**, 1039–1059, <https://doi.org/10.1175/JAMC-D-18-0211.1>.
- Plant, W. J., 1982: A relationship between wind stress and wave slope. *J. Geophys. Res.*, **87**, 1961–1967, <https://doi.org/10.1029/JC087iC03p01961>.
- Reichl, B. G., T. Hara, and I. Ginis, 2014: Sea state dependence of the wind stress over the ocean under hurricane winds. *J. Geophys. Res. Oceans*, **119**, 30–51, <https://doi.org/10.1002/2013JC009289>.
- Skamarock, W. C., and Coauthors, 2008: A description of the Advanced Research WRF version 3. NCAR Tech. Note NCAR/TN-475+STR, 113 pp., <https://doi.org/10.5065/D68S4MVH>.
- , and Coauthors, 2019: A description of the Advanced Research WRF Model version 4. NCAR Tech. Note NCAR/TN-556+STR, 145 pp., <https://doi.org/10.5065/1dfh-6p97>.
- Sullivan, P. P., J. C. McWilliams, and C.-H. Moeng, 2000: Simulation of turbulent flow over idealized water waves. *J. Fluid Mech.*, **404**, 47–85, <https://doi.org/10.1017/S0022112099006965>.
- , J. B. Edson, T. Hristov, and J. C. McWilliams, 2008: Large-eddy simulations and observations of atmospheric marine boundary layers above nonequilibrium surface waves. *J. Atmos. Sci.*, **65**, 1225–1245, <https://doi.org/10.1175/2007JAS2427.1>.
- , J. C. McWilliams, and E. G. Patton, 2014: Large-eddy simulation of marine atmospheric boundary layers above a spectrum of moving waves. *J. Atmos. Sci.*, **71**, 4001–4027, <https://doi.org/10.1175/JAS-D-14-0095.1>.
- , M. L. Banner, R. P. Morison, and W. L. Peirson, 2018a: Impacts of wave age on turbulent flow and drag of steep waves. *Procedia IUTAM*, **26**, 174–183, <https://doi.org/10.1016/j.piutam.2018.03.017>.
- , —, —, and —, 2018b: Turbulent flow over steep steady and unsteady waves under strong wind forcing. *J. Phys. Oceanogr.*, **48**, 3–27, <https://doi.org/10.1175/JPO-D-17-0118.1>.
- Talbot, C., E. Bou-Zeid, and J. Smith, 2012: Nested mesoscale large-eddy simulations with WRF: Performance in real test cases. *J. Hydrometeorol.*, **13**, 1421–1441, <https://doi.org/10.1175/JHM-D-11-048.1>.
- Wicker, L. J., and W. C. Skamarock, 2002: Time-splitting methods for elastic models using forward time schemes. *Mon. Wea. Rev.*, **130**, 2088–2097, [https://doi.org/10.1175/1520-0493\(2002\)130<2088:TSMFEM>2.0.CO;2](https://doi.org/10.1175/1520-0493(2002)130<2088:TSMFEM>2.0.CO;2).
- Wu, J., and L. Deike, 2021: Wind wave growth in the viscous regime. *Phys. Rev. Fluids*, **6**, 094801, <https://doi.org/10.1103/PhysRevFluids.6.094801>.
- , S. Popinet, and L. Deike, 2022: Revisiting wind wave growth with fully coupled direct numerical simulations. *J. Fluid Mech.*, **951**, A18, <https://doi.org/10.1017/jfm.2022.822>.
- Xiao, S., and D. Yang, 2019: Large-eddy simulation-based study of effect of swell-induced pitch motion on wake-flow statistics and power extraction of offshore wind turbines. *Energies*, **12**, 1246, <https://doi.org/10.3390/en12071246>.
- Yang, D., and L. Shen, 2009: Characteristics of coherent vortical structures in turbulent flows over progressive surface waves. *Phys. Fluids*, **21**, 125106, <https://doi.org/10.1063/1.3275851>.
- , and —, 2011a: Simulation of viscous flows with undulatory boundaries. Part I: Basic solver. *J. Comput. Phys.*, **230**, 5488–5509, <https://doi.org/10.1016/j.jcp.2011.02.036>.
- , and —, 2011b: Simulation of viscous flows with undulatory boundaries. Part II: Coupling with other solvers for two-fluid computations. *J. Comput. Phys.*, **230**, 5510–5531, <https://doi.org/10.1016/j.jcp.2011.02.035>.
- , C. Meneveau, and L. Shen, 2013: Dynamic modelling of sea-surface roughness for large-eddy simulation of wind over

- ocean wavefield. *J. Fluid Mech.*, **726**, 62–99, <https://doi.org/10.1017/jfm.2013.215>.
- , —, and —, 2014a: Effect of downwind swells on offshore wind energy harvesting—A large-eddy simulation study. *Renewable Energy*, **70**, 11–23, <https://doi.org/10.1016/j.renene.2014.03.069>.
- , —, and —, 2014b: Large-eddy simulation of offshore wind farm. *Phys. Fluids*, **26**, 025101, <https://doi.org/10.1063/1.4863096>.
- Zhang, W.-Y., W.-X. Huang, and C.-X. Xu, 2019: Very large-scale motions in turbulent flows over streamwise traveling wavy boundaries. *Phys. Rev. Fluids*, **4**, 054601, <https://doi.org/10.1103/PhysRevFluids.4.054601>.